Contributions to Mineralogy and Petrology (2020) 175:115
https://doi.org/10.1007/s00410-020-01746-5

ORIGINAL PAPER

Evidence for superhydrous primitive arc magmas from mafic enclaves at Shiveluch volcano, Kamchatka

Andrea E. Goltz[1] · Michael J. Krawczynski[1] · Maxim Gavrilenko[1,2,3,4] · Natalia V. Gorbach[5] · Philipp Ruprecht[2]

Received: 5 March 2020 / Accepted: 7 October 2020 / Published online: 18 November 2020

Abstract

Mafic enclaves preserve a record of deep differentiation of primitive magmas in arc settings. We analyze the petrology and geochemistry of mafic enclaves from Shiveluch volcano in the Kamchatka peninsula to determine the differentiation histories of primitive magmas and to estimate their pressures, temperatures, and water contents. Amphibole inclusions in high forsterite olivine suggest that the primitive melt was superhydrous (i.e., > 8 wt% H_2O) and was fractionating amphibole and olivine early on its liquid line of descent. We find that the hydrous primitive melt had liquidus temperatures of 1062 ± 48 °C and crystallized high Mg# amphibole at depths of 23.6–28.8 km and water contents of 10–14 wt% H_2O. The major and trace element whole-rock chemistry of enclaves and of published analyses of andesites suggest that they are related through fractionation of amphibole-bearing assemblages. Quantitative models fractionating olivine, clinopyroxene, and amphibole reproduce geochemical trends defined by enclaves and andesites in variation diagrams. These models estimate 0.2–12.2% amphibole fractionated from the melt to reproduce the full range of enclave compositions, which overlaps with estimates of the amount of amphibole fractionated from parental melts based on whole-rock dysprosium contents. This contribution extends the published model of shallow processes at Shiveluch to greater depths. It provides evidence that primitive magmas feeding arc volcanoes may be more hydrous than estimated from other methods, and that amphibole is an important early fractionating phase on the liquid line of descent of superhydrous, primitive mantle-derived melts.

Keywords Subduction zone volcanism · Shiveluch volcano · Kamchatka · Petrology · Superhydrous magma · Mafic enclaves

Introduction

Mafic enclaves are often intermixed with andesites at arc volcanoes and record magmatic processes that are largely "overwritten" by fractionation, assimilation, and mixing processes affecting the host andesite (e.g., Eichelberger et al. 2000; Izbekov et al. 2004; Browne et al. 2006; Halama et al. 2006; Plail et al. 2014, 2018). The presence of mafic enclaves in an andesite is a physical piece of evidence that mafic magma was involved in magma mixing (e.g., Eichelberger 1975; Bacon 1986). Studies of mafic enclaves themselves have revealed details about both shallow and deep mixing processes (e.g., Browne et al. 2006; Ruprecht et al. 2012; Plail et al. 2014), the role of mafic recharge in eruption catalysis (e.g., Martin et al. 2006, 2008; Ruprecht and Bachmann 2010; Plail et al. 2018), and the structure of magmatic plumbing systems at depth (e.g., Ruprecht et al. 2012; Davydova et al. 2017), thus complementing the information from host magmas. In this study, we examine the petrology

Communicated by Othmar Müntener.

Electronic supplementary material The online version of this article (https://doi.org/10.1007/s00410-020-01746-5) contains supplementary material, which is available to authorized users.

✉ Andrea E. Goltz
agoltz@wustl.edu

[1] Department of Earth and Planetary Sciences, Washington University in St. Louis, St. Louis, MO, USA

[2] Department of Geological Sciences and Engineering, University of Nevada, Reno, Reno, NV, USA

[3] Skolkovo Institute of Science and Technology, Moscow, Russia

[4] Vernadsky Institute of Geochemistry and Analytical Chemistry, Moscow, Russia

[5] Institute of Volcanology and Seismology, Russian Acadamy of Science, Petropavlovsk-Kamchatsky, Russia

and geochemistry of mafic enclaves recently erupted from Shiveluch volcano in Kamchatka. We use a combination of mineral chemistry and bulk rock major and trace element analyses to estimate the pressures, temperatures, and magmatic water contents of primitive Shiveluch magmas.

Holocene Shiveluch eruptions are dominated by andesites, and amphibole phenocrysts in the erupted andesites preserve a complex history of recharge by partially crystalline basaltic magmas in a shallow magma reservoir (e.g., Volynets et al. 1997; Dirksen et al. 2006; Humphreys et al. 2006, 2008; Ponomareva et al. 2007b; Ferlito 2011; Gorbach and Portnyagin, 2011; Gorbach et al. 2013, 2016). Shiveluch is of particular interest because its magmas are thought to be extremely hydrous (e.g., Portnyagin et al. 2007), with some estimates of water content as high as 6 wt% H_2O (Gavrilenko et al. 2016a), making it one of the most hydrous volcanoes in the world, comparable to Mt. Shasta in the Cascade Arc. (e.g., Baker et al. 1994; Grove et al. 2003, 2005). In this study, we present a model of lower crustal magmatism at Shiveluch before magmatic differentiation to andesite and show that fractional crystallization of olivine, clinopyroxene, and amphibole from a basaltic andesite parental melt reproduces the composition of enclaves and andesites erupted from Shiveluch. We conclude that high magmatic water contents are required to produce the mafic enclaves and their mineralogy. We estimate that differentiation processes occurring in the mid to lower crust require water contents of 10–14 wt%.

Geologic background

Shiveluch volcano is an eruptive center in the Kamchatka peninsula in Far Eastern Russia. The Kamchatka arc is located at the junction of the North American, Okhotsk, and Pacific plates (e.g., Bird 2003). Shiveluch is part of the northernmost segment of the arc called the Central Kamchatka Depression (CKD; e.g., Portnyagin et al. 2007). Volcanoes in the CKD are some of the most productive arc volcanoes on Earth (Fedotov 1991). Volcanic rocks along the CKD compositionally range from high-Mg basalts to dacites or rhyolites, although rhyolites are rare and basalts and andesites are the most frequently erupted in the CKD (e.g., Volynets 1991; Ponomareva et al. 2007a; Portnyagin et al. 2007; Churikova et al. 2013).

Shiveluch is the northernmost active volcano in the CKD. It is composed of two overlapping eruptive centers: Old Shiveluch (3283 m a.s.l; Ponomareva et al. 2007b) and Young Shiveluch (2800 m a.s.l; Ponomareva et al. 2007b; Fig. 1). Old Shiveluch is a Pleistocene-age stratovolcano inferred to have collapsed in a catastrophic eruption in the Late Pleistocene (Gorbach et al. 2013). The Young Shiveluch volcanic center is located within the crater formed by the catastrophic collapse of Old Shiveluch. Young Shiveluch has been active since the early Holocene (e.g., Volynets et al. 1997; Belousov et al. 1999; Gorbach and Portnyagin 2011; Ponomareva et al. 2015). Volcanism at Young Shiveluch includes 60 large Plinian eruptions throughout its history and frequent dome collapses followed by periods of regrowth (e.g., Belousov et al. 1999; Ponomareva et al. 2007a, 2015). The volcano normally erupts andesite, but throughout its history, there have been at least two instances of Mg-rich basaltic to basaltic-andesite eruptions identified in tephra deposits dated to 3959 (basaltic) and 8363 (basaltic andesite) BP (e.g., Volynets 1991; Volynets et al. 1997; Ponomareva et al. 2007a, 2015).

Our enclaves were collected from pyroclastic flows that occurred in 2005, 2010, and 2016 (coordinates of sample locations are reported in Supplementary Table 1 and shown graphically in Fig. 1) from the Young Shiveluch eruptive center. The pyroclastic flows are mostly composed of andesite from collapsed exogenous domes; whole rock and mineral geochemistry of the andesites in these flows is described in Gorbach et al. (2016). To summarize, the andesite is plagioclase and hornblende phyric. The plagioclase in andesites is on average $An_{40–50}$ and the amphibole is mostly 7–9 wt% Al_2O_3, but amphibole from pyroclastic deposits from 2007–2008 extends up to 14 wt% Al_2O_3. Gorbach et al. (2016) estimate an average eruption temperature of 847 ± 18 °C and a maximum temperature of 970 °C using the hornblende thermometer of Ridolfi et al. (2010) and the amphibole-plagioclase thermometer of Holland and Blundy (1994). The enclaves range in size from nearly single crystals up to 0.4 m in their diameter, but only enclaves > 10 cm in size were collected. Most enclaves are elliptical and have crenulated margins, while some have sharper, more angular brecciated boundaries.

Analytical methods

Whole-rock chemical analysis

Fourteen samples were prepared for whole-rock analyses first by crushing. Crushed fragments were then boiled in deionized water for ~ 20 min and dried. Fragments of the enclave were hand-selected to avoid hammer marks, saw cuts, and any fragments of host andesite. Whole-rock major element compositions of 14 samples were determined by X-ray Fluorescence spectrometry (XRF) using the Thermo-ARL automated spectrometer at Washington State University following methods of Johnson et al. (1999); one sample, 17-02B, was analyzed in duplicate to assess precision and sample homogeneity. Glass beads for XRF analysis were prepared from ~ 3.5 g of crushed rock sample with 7 g of $Li_2B_4O_7$ flux. Trace elements were analyzed using inductively coupled plasma mass spectrometry (ICP-MS)

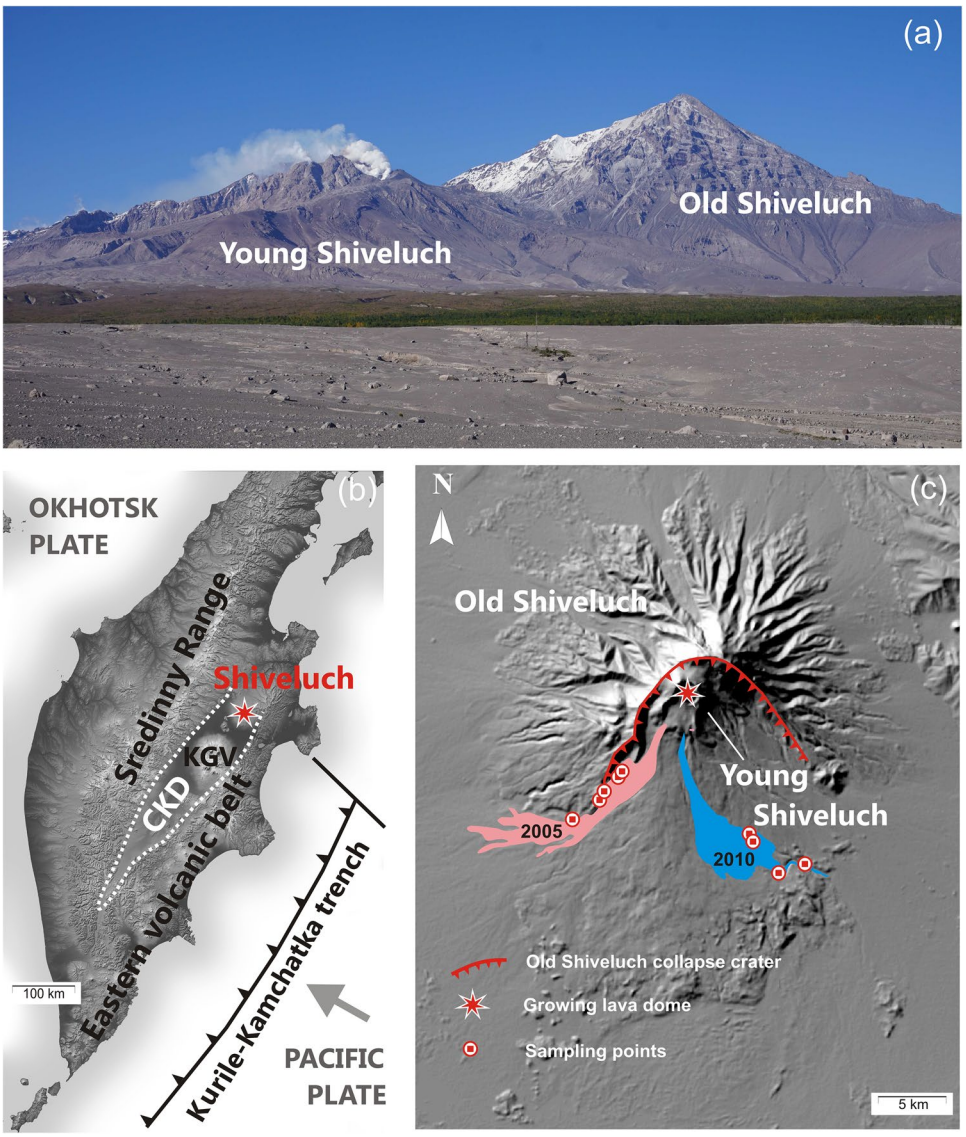

Fig. 1 **a** Image of Old and Young Shiveluch. **b** Map of regional geology, including of the Central Kamchatkan Depression (CKD) which includes the Klyuchevskoy Group Volcanoes (KGV) and Shiveluch in the north. **c** Aerial view of Shiveluch outlining the 2005 and 2010 flows from the Young Shiveluch center. Sampling points of enclaves presented in this study (also found in Supplementary Table 1) are shown. The 2016 flow from the Young Shiveluch center covers areas of the 2005 flow

at Washington State University on an Agilent model 4500 ICP-MS following the method of Knaack et al. (1994).

Electron microprobe composition microanalysis

Microprobe analysis was performed on a JEOL JXA-8200 electron microprobe equipped with 5 wavelength-dispersive spectrometers. Analyses were acquired using the Probe for EPMA software (Donovan et al. 2012); background correction was performed using a mean atomic number (MAN) correction (Donovan and Tingle 1996); and corrections for atomic number, X-ray absorption, and secondary fluorescence (ZAF, collectively) were performed using the CITZAF software (Armstrong et al. 2013). Analytical conditions for mineral analyses were: 15 kV accelerating potential, 1–5 µm beam diameter, and 25 nA probe current (see Electronic Supplementary Material for more details). The instrument was standardized for the analysis of Si, Ti, Mg, Al, Mn, Fe, Cr, Ni, Ca, Na, and K before the run using primary standards and other secondary standards for the MAN correction (e.g., Donovan et al. 2012). The accuracy of the standardization was corrected for drift by periodic analyses of the secondary standard Kakanui Hornblende (Smithsonian standard USNM 143956; Jarosewich et al. 1980) throughout the analytical session.

Measurements of trace Al in olivine were acquired using a 150 nA probe current and a 3 µm beam diameter. Al was measured simultaneously on two spectrometers (both using the TAP crystal) using 100 s on-peak count times; reported aluminum is the amalgamated value from both spectrometers. The Mg, Si, Fe, Mn, P, Ni, Ti, and Cr content of olivine grains used in Al-in-olivine thermometry were also measured with the 150 nA probe current and had a MAN background correction applied. Background corrections for

Al in olivine were performed using a conventional polynomial background method because of the low concentration of Al in olivine (as shown by Batanova et al. (2015) to be a successful approach). The modeled background was based on wavescans on both spectrometers of a synthetic forsterite standard, which has no aluminum. The limit of detection of Al_2O_3, determined by background levels of Al in synthetic forsterite, was 30 ppm. Several grains of San Carlos olivine (Smithsonian standard NMNH 111312-44) were measured as unknowns to assess the accuracy of our measurements. We closely reproduced the reported Al_2O_3 content of San Carlos olivine (320 ppm) in 8 measurements of several grains of San Carlos olivine (on average 302 ppm with 0.5 to 15% deviation from the standard; Electronic Supplementary Material).

Results

Petrography and mineral chemistry of mafic enclaves

Enclave petrography

Enclaves have a micro-vesicular, aphyric to porphyritic texture. Modal mineral abundances were estimated from inspection of hand samples and thin sections. Most enclaves are dominated by amphibole and plagioclase, and zoning in these microphenocrysts is discussed in more detail in the following sections.

Enclaves are porphyritic to sparsely phyric with a phenocryst assemblage of olivine + amphibole ± clinopyroxene ± orthopyroxene ± plagioclase (Supplementary Fig. 1c–f). The matrix consists of glass and microcrystalline to fine-grained (100–200 µm) plagioclase and amphibole. Olivine is a common phenocryst and tends to have an outer

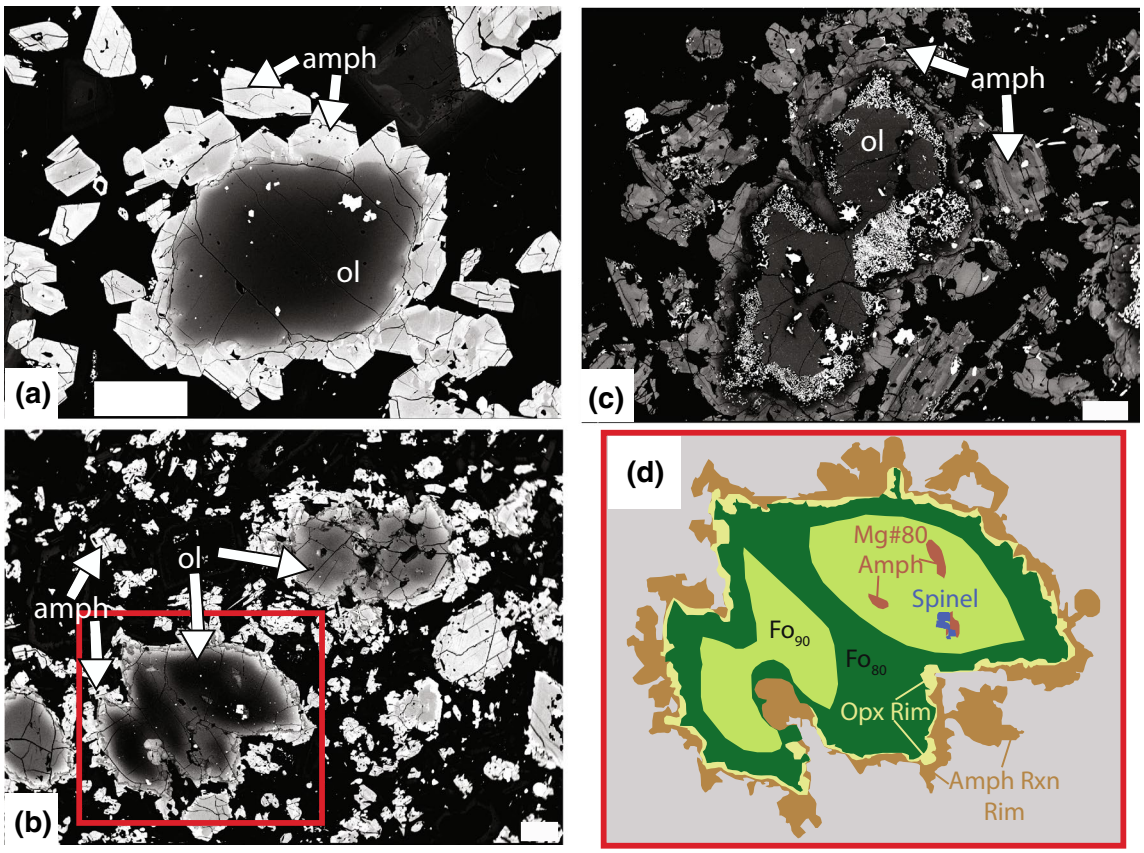

Fig. 2 BSE images of olivine phenocrysts. **a** Olivine grain from enclave 17-09. This grain lacks a reaction rim of orthopyroxene. It has an amphibole reaction rim. Scale bar is 200 µm. **b** Olivine grains from enclave 17-02B. The grain on the left (with a red square) has a thin orthopyroxene reaction rim; both grains pictured have an amphibole reaction rim. Scale bar is 200 µm. **c** Symplectite-rimmed olivine from enclave 17-04B. The grain is rimmed by amphibole. Scale bar is 200 µm. **d** Simplified line sketch of the olivine phenocryst in the red box in **b**. The grain is about 700 µm across in its long dimension. High magnesium amphibole inclusions (reddish brown), inner orthopyroxene reaction rim (yellow), and outer, lower Mg# amphibole reaction rim (brown) are highlighted. Lighter green color represents higher Fo olivine; darker green represents lower Fo olivine

reaction rim of high-Mg clinopyroxene and/or amphibole; some grains also have a thin inner reaction rim of high-Mg orthopyroxene or a thicker reaction rim of intergrown orthopyroxene and titanomagnetite (symplectite; Fig. 2). High forsterite olivine grains (i.e., Fo ≥ 88) contain inclusions of chromite and high-Mg amphibole (i.e., Mg# ≥ 74; Supplementary Table 2, Supplementary Fig. 2).

In addition, two enclaves are classified as cognate xenoliths that are cumulate rocks (Supplementary Fig. 1a, b), with an assemblage of clinopyroxene + amphibole + plagioclase ± orthopyroxene. The two cumulate enclaves presented here are texturally and geochemically distinct. The more magnesian cumulate, 17-16B, is richer in cpx than 17-04L. Some amphibole grains in the cumulates have inclusions of clinopyroxene in their cores, and plagioclase occurs interstitially. The mineralogy of sample 17-04L was determined by mass balance (Electronic Supplementary Material), and is 59% amphibole, 20% An_{85}, 14% An_{63}, 4% titanomagnetite, 2% clinopyroxene, and 0.9% apatite. The distribution of these minerals is heterogeneous in the sample; some areas are nearly 100% amphibole with minor clinopyroxene and titanomagnetite, and those are surrounded by a matrix dominated by plagioclase.

Olivine

Olivine chemistry differs among enclave samples (Supplementary Table 3). Olivine grains in some enclaves are normally zoned, with high magnesium cores (Fo_{85}-Fo_{92}) and lower magnesium rims (Fo_{77}-Fo_{83}) (Figs. 2a, b, 3a). In

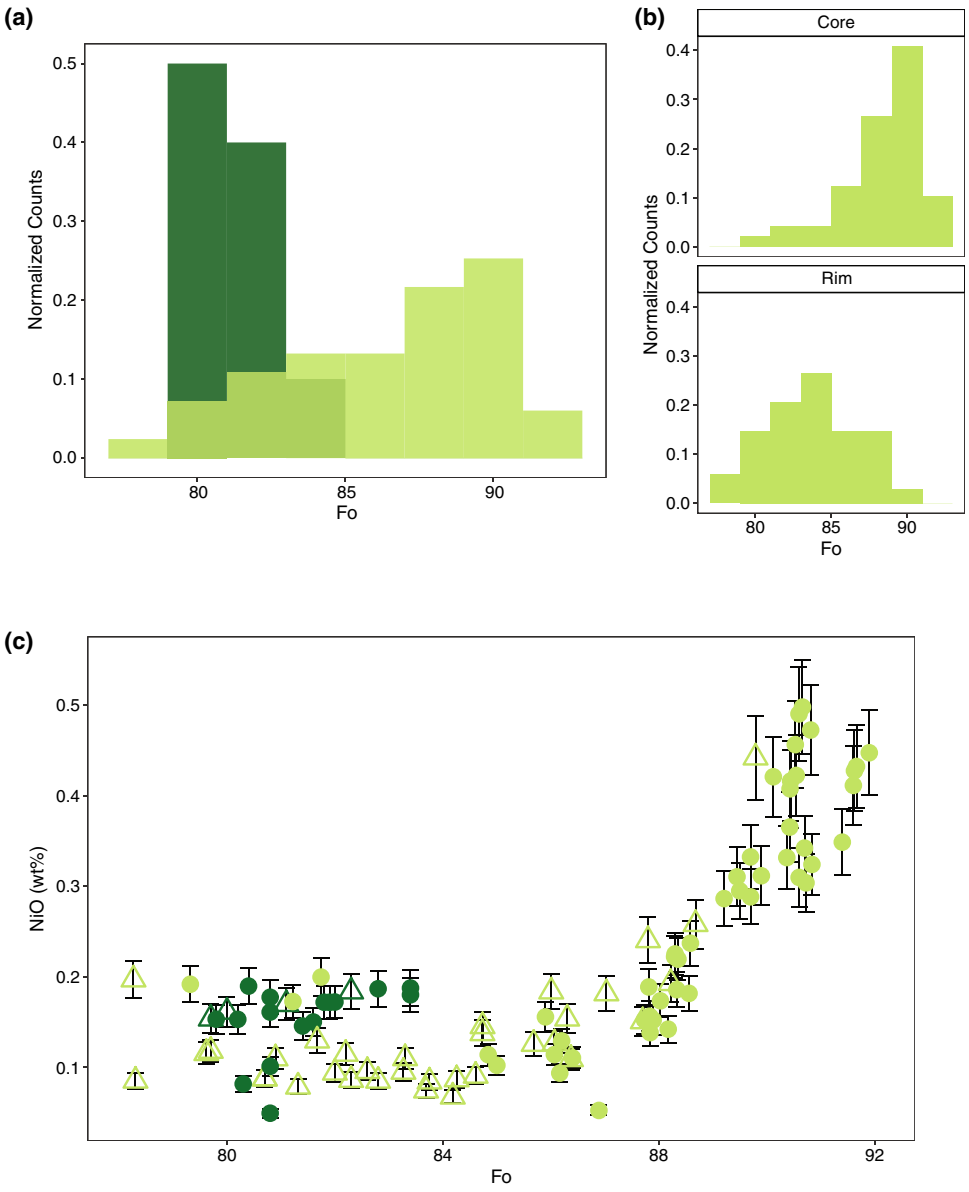

Fig. 3. **a** Forsterite content of microprobe analyses of olivine from quenched enclaves. Lighter green indicates normally zoned olivine (n = 79); darker green are analyses of olivine with symplectite rim (n = 24). **b** Histograms of forsterite content of olivine cores (above; n = 46) and rims (below; n = 33) in normally zoned olivine. **c** Forsterite content vs. NiO wt% of olivine grains from microprobe analysis with error bars. In this plot, circles represent core analyses and triangles are rim analyses

some samples, olivine is significantly less zoned with cores and rims compositionally clustered at Fo_{79}-Fo_{83} (Figs. 2c, 3a). These olivines are lower in CaO and higher in NiO than zoned olivine (Supplementary Table 3; Fig. 3). They also characteristically have an inner reaction rim of a symplectite intergrowth of orthopyroxene and titanomagnetite (Fig. 2c). We interpret them as xenocrystic in the enclaves based on the similar composition of these unzoned olivines and olivines in xenoliths erupted at Shiveluch (in particular, the low calcium content of 0.03 wt% on average in the xenoliths and the enclaves; e.g., Bryant et al. 2007; Gavrilenko et al. 2016a; Gorbach pers. comm.). In zoned olivine, NiO content in olivine analyzed across all samples decreases with decreasing forsterite content up to Fo_{85}, at which point NiO in olivine plateaus at NiO 0.1–0.2 wt% (Fig. 3b).

Amphibole

All analyzed amphiboles are in the edenite to pargasite range by the calculation and nomenclature of Leake et al. (1997). For simplicity, we will use the term amphibole regardless of classification. Amphibole occurs as a phenocryst phase (Fig. 4), as a reaction rim around olivine phenocrysts (Fig. 2), and as inclusions in olivine phenocrysts that span the range of reported Fo content (Supplementary Table 2) and plagioclase xenocrysts.

Amphibole phenocrysts range in Mg# from 56–82. In this study, we report Mg# assuming that all Fe is Fe^{2+}. This assumption is flawed, especially because Fe^{3+} should readily partition into amphibole (e.g., Dalpé and Baker 2000; King et al. 2000). However, we do not use EMPA data to estimate Fe^{3+} because measured values of Fe^{3+} using Mossbauer or micro-XANES techniques do not correlate with calculated values of Fe^{3+} from microprobe analyses, especially given unknown occupancy of the O3 site (i.e., without precise hydrogen and halogen analyses; e.g., Dyar et al. 1992, 1993,

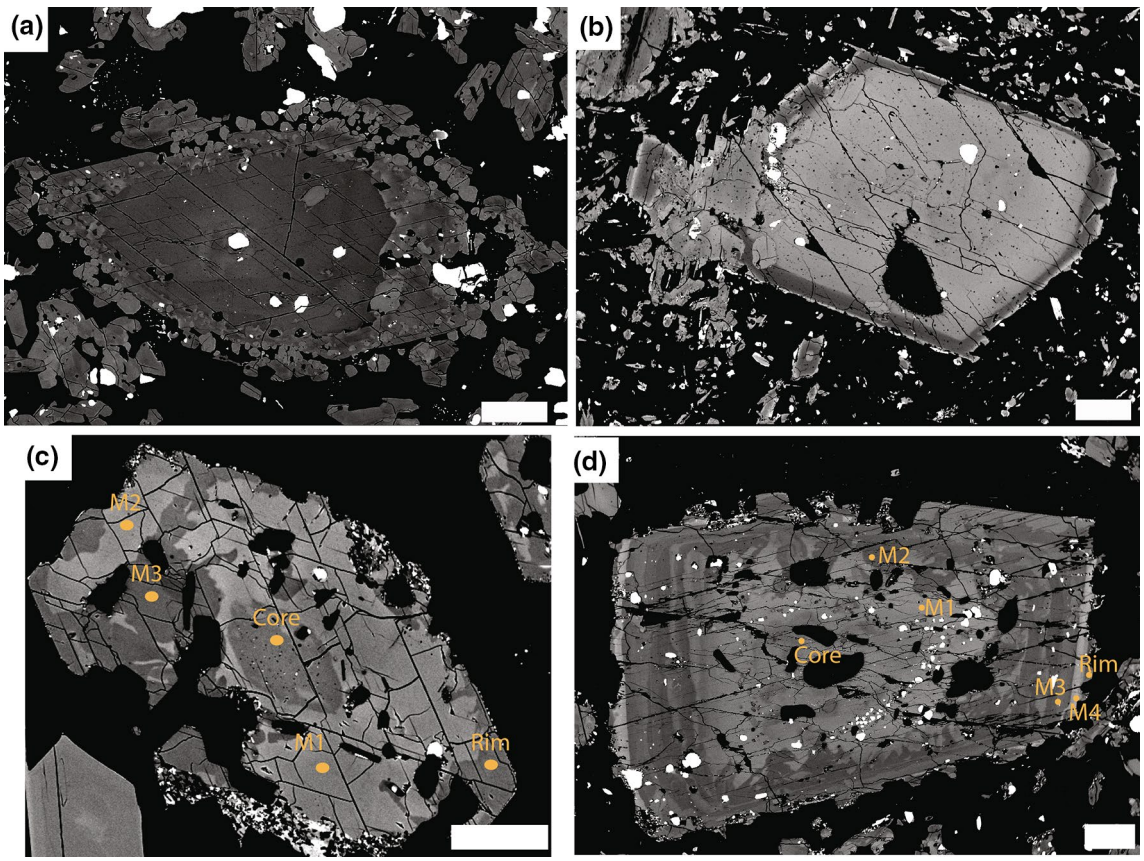

Fig. 4 BSE images of amphibole phenocrysts. Labels in **c** and **d** correspond to compositions reported in Supplementary Table 4. **a** Normally zoned phenocryst. The rim of this grain is host to many clinopyroxene inclusions. Scale bar is 100 µm. **b** Reversely zoned phenocryst. Scale bar is 200 µm. **c** Patchy zoned phenocryst. Scale bar is 100 µm. **d** Multiply zoned phenocryst. The core is host to plagioclase (black in this image) and titanomagnetite (brighter grains) inclusions. Scale bar is 200 µm

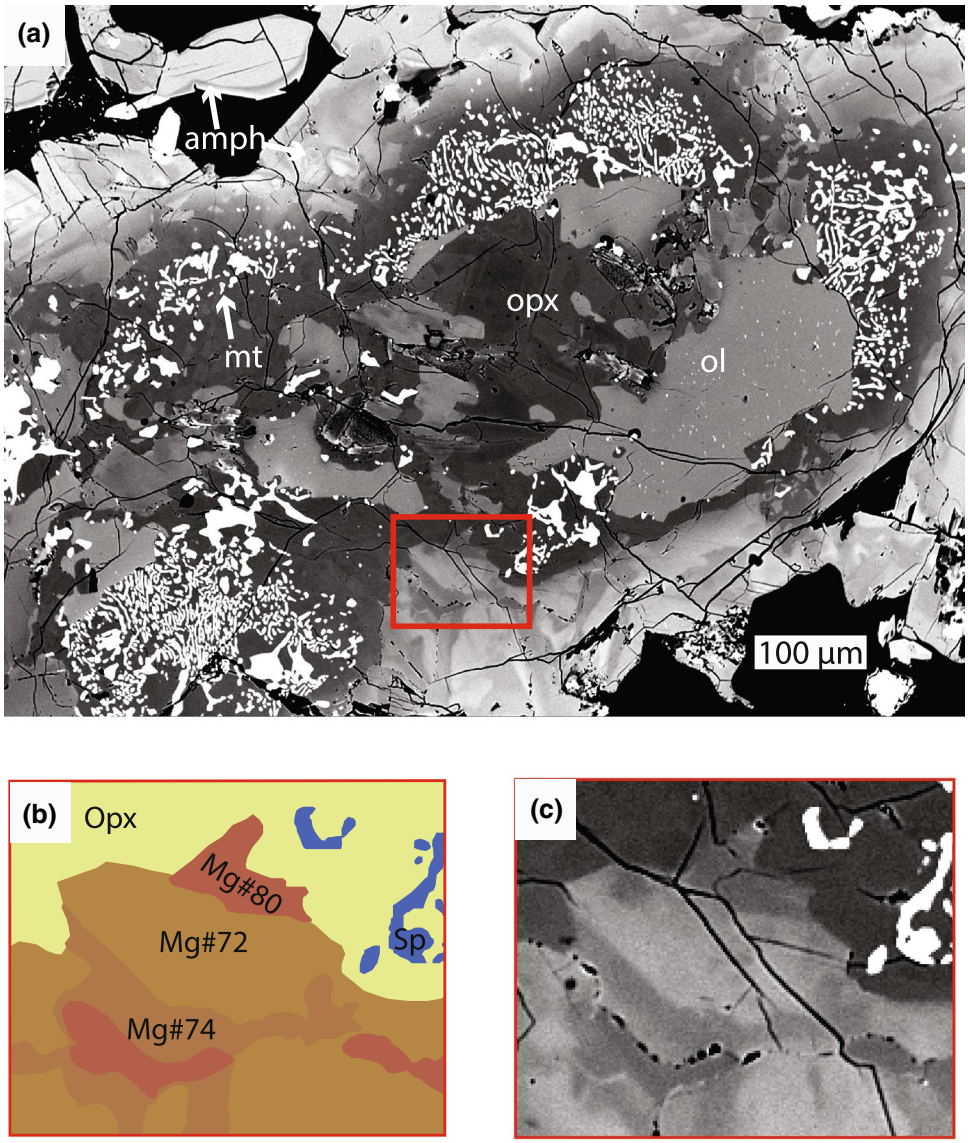

Fig. 5 **a** BSE image of heavily reacted symplectite grain. **b** Line diagram of outer amphibole reaction rim (brown/orange) and inner orthopyroxene reaction rim from area outlined in red in **a**. **c** BSE image of the area depicted in **b**

2016; Delaney et al. 1998; King et al. 1999, 2000). We chose not to consider Fe^{3+} in our reported amphibole Mg# to avoid the unconstrained uncertainty associated with estimating Fe^{3+} from our microprobe analyses.

There are three categories of Mg-Fe amphibole zoning in enclave phenocrysts: normal, reverse, and complex (Fig. 4; representative analyses may be found in Supplementary Table 4). Complex zoning in this context refers either to patchy zoning or "multiple zoning" meaning that the amphibole has thick, irregularly spaced bands of variable magnesium and/or aluminum content. All enclaves have a higher abundance of reversely or complexly zoned amphiboles than normally zoned amphibole phenocrysts, which are rare but do occur. Amphibole reaction rims around olivine are often polycrystalline and normally zoned with high Mg# amphibole in grain cores, ranging from 63–81. Some amphibole reaction rims around low forsterite olivine grains have Mg# up to 80 (Fig. 5).

Amphibole ranges in Al_2O_3 from 5 to 17 wt% (Fig. 6). In general, the aluminum content of an amphibole increases with decreasing amphibole Mg#. This is most pronounced for amphiboles with Mg# < 74. Enclaves have amphibole phenocrysts and amphibole with high magnesium number inclusions in olivine (i.e., Mg# > 74), and high magnesium amphiboles have highly variable aluminum content (> 10 wt% range; Fig. 6).

Amphibole is included with plagioclase, titanomagnetite, orthopyroxene, clinopyroxene, and rarely apatite. Apatite and plagioclase inclusions occur in amphibole with Mg# < 74, and typically in the cores of those amphiboles. The chemistry of plagioclase inclusions in amphibole is discussed further in the following sections.

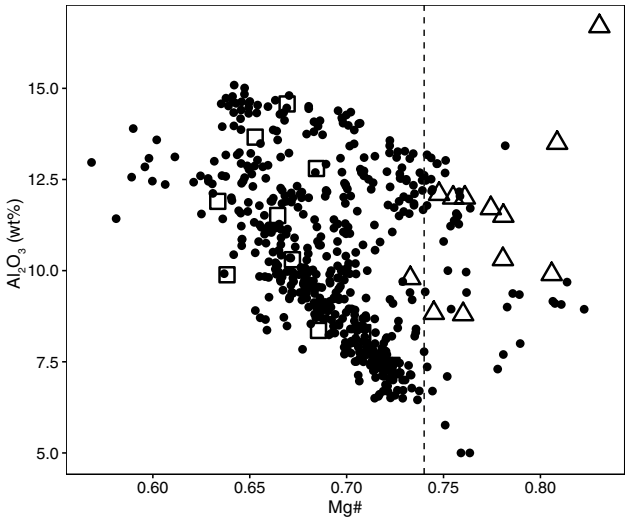

Fig. 6. Amphibole phenocryst variation diagram in Al_2O_3. Open triangles represent analyses of inclusions of amphibole in olivine and open squares represent analyses of inclusions of amphibole in plagioclase. Dashed line is placed at Mg# = 74; analyses to the right of the line were those used in amphibole barometry

Pyroxene

Clinopyroxene occurs as a phenocryst phase, a reaction rim around olivine phenocrysts in some enclaves, and as inclusions in amphibole and plagioclase. Clinopyroxene phenocrysts are rare, but those that are present are relatively small (~ 400 µm) and normally zoned from core to rim. Clinopyroxene phenocryst cores range from $En_{51}Wo_{38}$ to $En_{44}Wo_{46}$ (Mg# 62–89) (Supplementary Fig. 3; Supplementary Table 5). Rims range from $En_{45}Wo_{42}$ to $En_{42}Wo_{45}$ (Mg# 66–80). All clinopyroxene inclusions in other phenocryst phases closely resemble compositions of clinopyroxene phenocryst rims.

Orthopyroxene is rare or absent as a phenocryst phase. Analyzed phenocrysts are unzoned, but crystal-to-crystal variation spans in Mg# from 64 to 75 ($En_{73.1–70.1}Wo_{1.6–1.8}$). More magnesian orthopyroxene occurs as a component of symplectite reaction rims around lower magnesium olivine grains ($En_{79-83.5}Wo_{0.8–2.1}$; Mg# 79–84).

Plagioclase

Plagioclase in all enclaves either has sieve-textured cores (> 75% of all grains) and/or is oscillatory zoned (Supplementary Fig. 4). Sieve-textured plagioclase grains have calcium-poor (An_{33}-An_{50}) cores. Rims around the sieve-textured cores are normally zoned from An_{50}-An_{78} near the core to An_{38}-An_{40} near the rim (Supplementary Fig. 4a, c, d; Supplementary Fig. 5; Supplementary Table 6). Oscillatory zoned plagioclase grains have cores of ~ An_{45} and have variations in An content of < 20 mol% along a core-rim transect (Supplementary Fig. 4b; Supplementary Fig. 6). Oscillatory zoned plagioclase is rare in the enclaves, and we interpret it to be xenocrystic because of its rarity and because its An content is lower than the An content of the cores of groundmass plagioclase. Plagioclase is also the major groundmass phase in all non-cumulate enclaves. Groundmass plagioclase is normally zoned with cores of An_{52}-An_{68} and rims of An_{17}-An_{41}. The composition of the groundmass plagioclase is similar to the rims of sieve-textured plagioclase, suggesting co-crystallization.

Plagioclase inclusions are found in the cores of complex or reverse zoned amphiboles (Fig. 4d). On average, the plagioclase inclusions in amphibole are An_{50}, and plagioclase including amphibole is on average An_{52}. The average composition of plagioclase inclusions in amphibole closely approximates the composition of the cores of groundmass plagioclase, the inner rim of patchy plagioclase, and oscillatory-zoned plagioclase in the host andesite.

Whole-rock chemical analysis

The major element compositions of the enclaves range from 6.74 to 10.68 wt% in MgO, 51.96 to 56.31 wt% in SiO_2, and from 15.01 to 16.03 wt% in Al_2O_3 (Fig. 7; Supplementary Table 7). The enclaves are high-Mg# basaltic andesites. Non-cumulate enclaves range in magnesium number from 60 to 69.1 (using data normalized to 100% and considering Fe as FeO_{total}) (Supplementary Table 7; Electronic Supplementary Material). The compositions are some of the most magnesian reported from Young Shiveluch; other high magnesium materials are the basaltic to basaltic-andesite tephras, which both have Mg# 69 (MgO = 9.51, 10.76 wt% for the 8363 and 3959 BP tephras, respectively; e.g., Volynets et al. 1997; Ponomareva et al. 2007b) and a phlogopite-bearing basalt found in the Western crest of the main caldera (Gorbach and Portnyagin 2011; sample 7550-1, Mg# = 71.7, MgO = 11.82 wt%).

Together, the enclaves define crystallization-dominated trends in most bivariate plots (Fig. 7). The enclave data extend trends defined by published analyses of andesites erupted at Young Shiveluch (Hochstaedter et al. 1996; Ishikawa et al. 2001; Ferlito 2011; Gorbach and Portnyagin 2011) to more magnesian compositions without a compositional gap. The dataset (i.e., enclaves and andesites) increases in SiO_2, K_2O, Al_2O_3, Na_2O, Sr, Ga, Rb, Ba, and Zr with decreasing MgO (Fig. 7; Supplementary Fig. 7). The trends in FeO, CaO, TiO_2, Cr, Ni, and V are decreasing with decreasing MgO. There is no distinguishable trend in Zn, or Y. P_2O_5 increases to MgO ~ 5 wt% and then decreases.

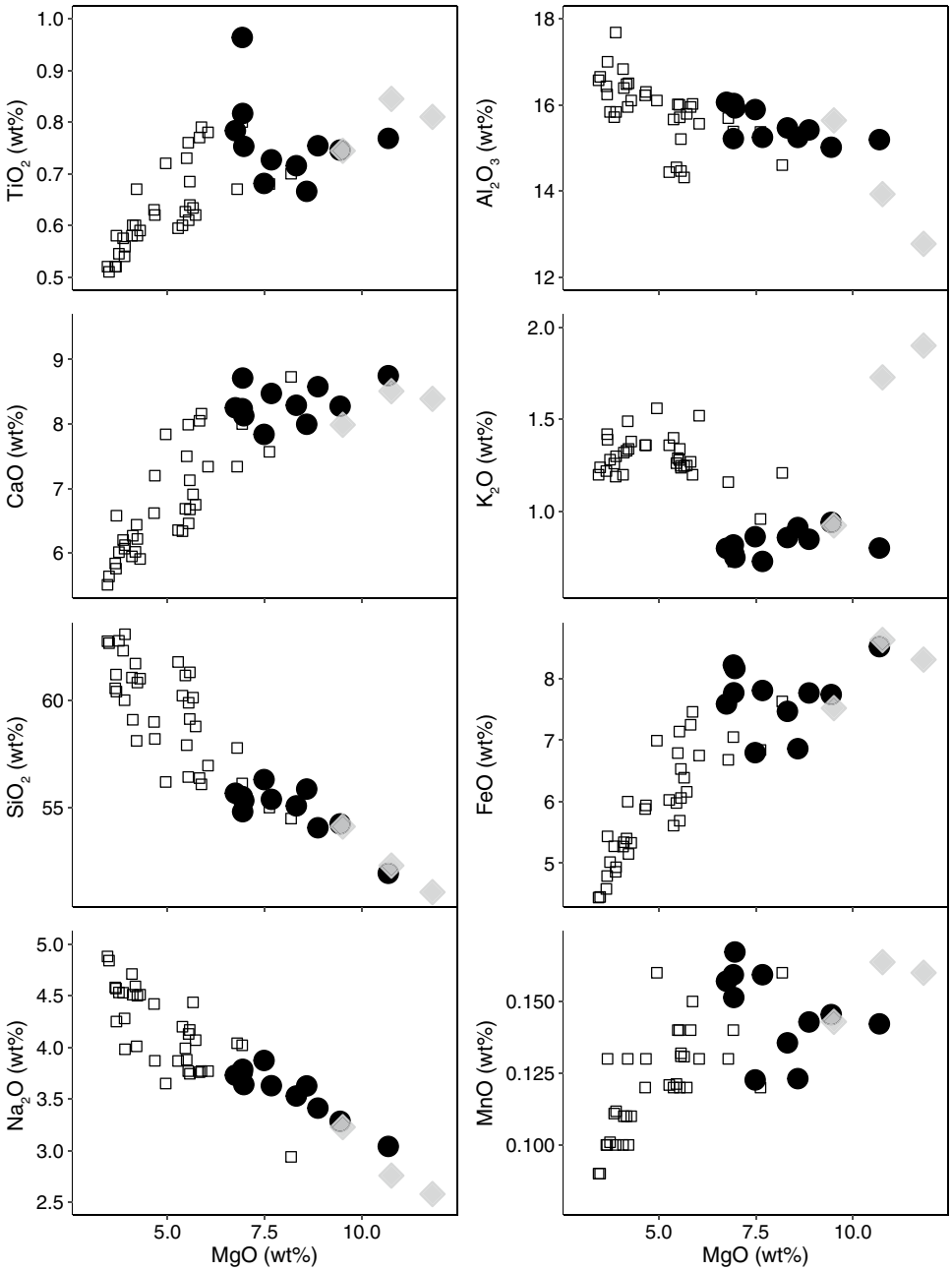

Fig. 7 Selected major element variation (Harker) diagrams. Circles represent enclave analyses from this study; open black squares are published analyses of andesite from Gorbach and Portnyagin (2011), Hochstaedter et al. (1996), Ishikawa et al. (2001), and Ferlito (2011); grey diamonds are compositions of tephra from Ponomareva et al. (2007a) and a high Mg# basalt from Gorbach and Portnyagin (2011)

Trace element (ICP-MS) analysis

This study is the first comprehensive report of trace element compositions of Shiveluch mafic enclaves. The normalized REE patterns of the mafic enclaves are relatively flat in the LREE (Fig. 8a, b); the ratio of $(La/Nd)_N$ has a narrow range of 1–1.3 in all enclaves except for amphibole cumulate sample 17-04L, where $(La/Nd)_N = 0.8$ (Supplementary Table 7). There is a weak negative correlation of $(La/Nd)_N$ with MgO (Supplementary Fig. 8).

Overall, the REE patterns of the mafic enclaves are concave up. In this study, we quantify the curvature of the normalized REE pattern using the Dy/Dy^* index proposed by Davidson et al. (2013) as opposed to the La/Yb index (although those values are also reported in Supplementary Table 7). Dy^* is defined as the interpolated value of Dy from a line with endpoints at La and Yb. A Dy/Dy^* value < 1 indicates a concave up curve. The mafic enclaves range in Dy/Dy^* from 0.88 to 1 (± 0.04) except for cumulate sample 17-04L which has a Dy/Dy^* value of 1.27. There is a weak positive correlation of Dy/Dy^* with enclave whole-rock magnesium content (Fig. 8c). We also determined the Eu/Eu^* values of these enclaves (Supplementary Table 7; Supplementary Fig. 8). Values range from 0.96–1.1 (± 0.04)

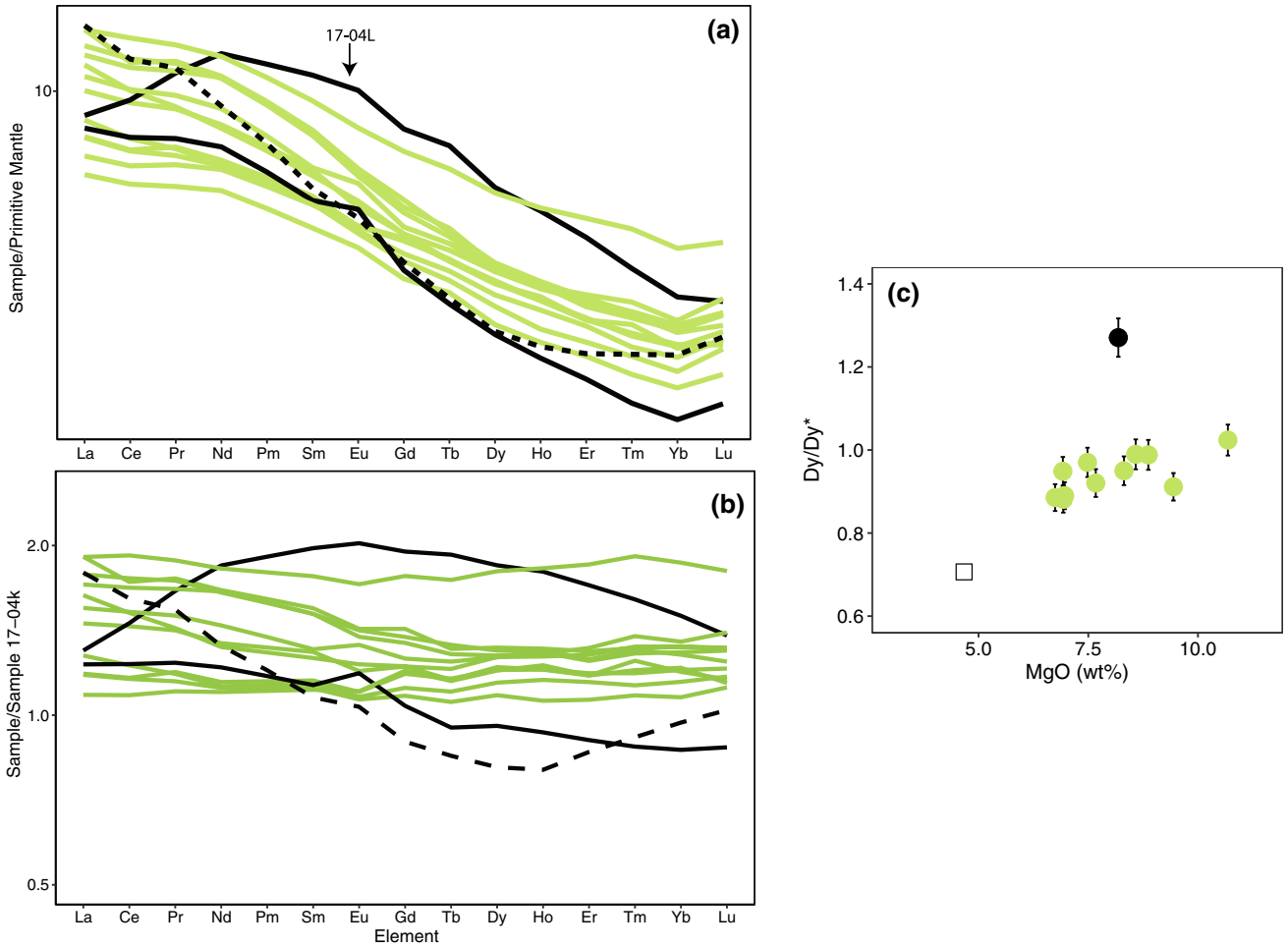

Fig. 8 Rare earth element abundances of analyzed enclaves. Element abundance has been normalized to Primitive Mantle (Sun and McDonough 1989) (**a**) and enclave 17-04K (**b**). **c** Dysprosium anomaly versus MgO of analyzed enclaves and of published analysis of andesite from Davidson et al. (2013). Solid black lines or points are analyses of cumulate samples, green lines or points are analyses of enclaves, and dashed black line or open squares from the ICP-MS analysis of Shiveluch andesite from Davidson et al. (2013). All analyses from this study have a precision of 5% relative standard deviation (RSD). Uncertainty in the dysprosium anomaly was calculated by propagating uncertainty from ICP-MS analysis of trace elements through the calculation of Dy/Dy*. Published data were reported without uncertainty, and thus the data are reported here without propagated uncertainty. There is a weak positive correlation between Dysprosium anomaly and MgO

across all enclaves, and there is no correlation of Europium anomaly with whole rock magnesium content.

Discussion

Intensive parameters of primitive magma crystallization

Temperature

Temperature is a key intrinsic condition in magmatic systems. In the absence of two oxide pairs or co-existing clinopyroxene and glass, the temperature of primitive arc magmas is difficult to determine. The temperature of magmas in equilibrium with high forsterite olivine was determined by employing the Aluminum-in-olivine thermometer of Coogan et al. (2014). The thermometer uses the chromium number of chromite in equilibrium with olivine and the aluminum partitioning between chromite and olivine pairs; this partitioning is sensitive to the temperature of crystallization. Although the thermometer of Coogan et al. (2014) (and an earlier calibration; Wan et al. 2008) was not calibrated for hydrous magmas, it has been applied to hydrous systems, including Shiveluch (e.g., Mironov et al. 2015; Gavrilenko et al. 2016b; Golowin et al. 2017; Gordeychik et al. 2018; Asafov et al. 2018).

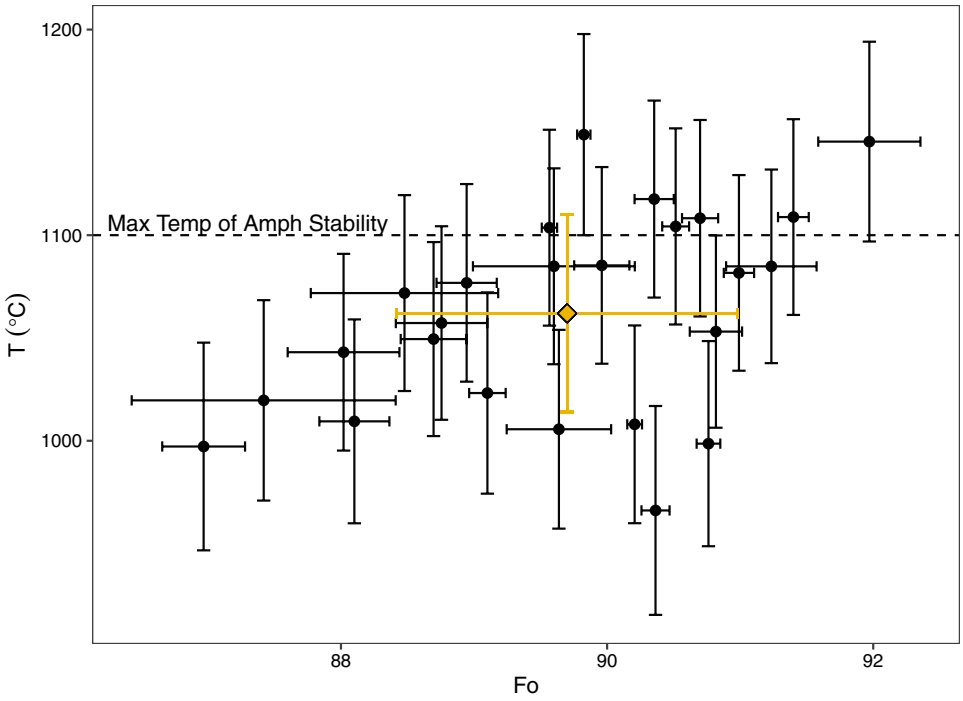

Fig. 9 Average temperatures of 25 olivine and chromite pairs from Al-in-olivine thermometry. Dashed line shows the approximate upper thermal stability limit of amphibole. Gold-colored point shows average temperature from all pairs (1062 ± 48 °C). All error bars show 1 sigma uncertainty. There is a minor correlation of temperature with forsterite content, but such minor variation is not considered further

Chromite inclusions in forsterite-rich olivine (i.e., Fo ≥ 86) were analyzed to determine the temperature of near-liquidus magmas at Shiveluch. For every chromite inclusion analyzed, three to five analyses of olivine were collected. Uncertainties were determined using a Monte Carlo technique, performing the calculation of temperature for each olivine analysis 10,000 times with a Gaussian distribution of values for Cr in chromite, Al in chromite, Al in olivine, and the coefficients in the equation of the thermometer of Coogan et al. (2014) within their uncertainties and finding the standard deviation of the repetitive calculation. Temperatures from chromite-olivine pairs were excluded from consideration if: (1) the 3–5 analyses of olivine for one chromite inclusion had a standard deviation ≥ 25 °C (the limiting precision of the Coogan et al. (2014) thermometer, not taking into account any uncertainties from EPMA) or (2) if the analytical precision of aluminum in olivine by EPMA was low. Points with low analytical precision had a percent error in temperature from uncertainty in EPMA measurements greater than the percent error of the thermometer (4%, as calculated by our Monte Carlo simulation; Supplementary Fig. 9). Of a starting dataset of 58 pairs, condition 1 filtered 28 pairs out, and condition 2 filtered out another five pairs. In total, 25 olivine-chromium pairs were considered robust estimates of temperature; analyses of olivine and chromite in those pairs are presented in the Electronic Supplementary Material and are graphically summarized in Fig. 9. The 25 pairs have an average temperature of 1062 ± 48 °C, and have minor variation with forsterite content (Fig. 9); this small variation is not further considered. The temperatures are mostly within the error of or below the upper thermal stability limit of amphibole, which is about 1100 °C (e.g., Helz, 1973; Blatter and Carmichael, 2000; Alonso-Perez et al. 2008; Krawczynski et al. 2012; Blatter et al. 2017). These low temperatures would thus be conducive to near-liquidus amphibole crystallization. As will be further discussed in the following section, near or at liquidus crystallization of amphibole requires high water contents to depress the liquidus temperature of primitive magmas.

Water content

We estimated the water content of primitive melts crystallizing amphibole by applying an amphibole Mg# geobarometer-hygrometer to amphiboles with Mg# ≥ 74 (assuming all iron is ferrous) for which the geobarometer-hygrometer is calibrated (Krawczynski et al. 2012; Table 1). Experimental studies have shown that amphibole crystallization occurs at near-liquidus temperatures in H_2O-saturated magmas because water lowers the liquidus temperatures, making them closer to the maximum temperatures of amphibole stability (e.g., Helz 1973). Grove et al. (2003, 2005) proposed a linear relationship between high Mg# amphibole and water content at a given f_{O_2}, and applied their hygrometer to high Mg# amphibole erupted at Mount Shasta. The experimental study of Krawczynski et al. (2012), based on and applied to high Mg# rocks from Mount Shasta, refined the empirical, nonlinear relationship between amphibole Mg# and water content at high pressures; we apply the equation from Krawczynski et al. (2012) to high Mg# amphiboles in

Table 1 Analyses of high Mg# amphibole and results from amphibole Mg# geobarometer-hygrometer, calculations of water content, and calculation of temperature applied to the 8 highest Mg# amphibole analyses

Sample	17-02B	17-02B	17-02B	17-02B	17-04K	17-04K	17-04K	17-04K	17-04K	17-05	17-05	17-05	17-05
SiO_2	44.85	41.33	46.73	42.85	46.81	45.53	45.26	43.96	47.60	43.20	46.60	46.87	46.72
TiO_2	1.38	1.98	1.69	1.80	1.23	0.67	1.02	1.87	1.17	1.10	1.90	0.19	0.23
Al_2O_3	11.71	16.74	8.83	13.58	9.69	11.27	11.22	11.57	8.84	13.18	8.94	10.31	9.96
FeO	8.60	5.96	9.72	7.06	7.21	9.34	9.49	9.24	8.51	9.93	9.72	8.90	9.69
MnO	0.15	0.08	0.24	0.06	0.08	0.18	0.15	0.09	0.19	0.11	0.21	0.18	0.19
MgO	16.58	16.38	17.25	16.62	17.67	16.41	16.30	16.13	13.95	15.99	16.71	17.78	17.37
CaO	10.66	11.56	9.98	11.82	11.69	11.70	11.33	11.60	15.92	11.48	11.32	10.96	11.05
Na_2O	2.57	3.08	2.29	3.00	2.11	2.29	2.24	2.51	1.31	2.64	1.95	2.17	2.04
K_2O	0.24	0.29	0.21	0.27	0.19	0.22	0.21	0.22	0.07	0.34	0.44	0.22	0.20
P_2O_5	0.04	0.04	0.16	0.03	< 0.01	0.04	0.01	0.04	< 0.01	0.01	0.03	0.06	0.07
Cr_2O_3	0.15	< 0.01	0.05	0.02	0.43	0.10	0.04	0.03	0.07	0.01	0.01	0.07	0.03
NiO	0.05	0.09	0.04	0.03	0.10	< 0.03	0.05	< 0.03	< 0.03	< 0.03	< 0.03	0.03	< 0.03
Total	96.97	97.54	97.19	97.15	97.20	97.75	97.33	97.26	97.60	97.99	97.85	97.74	97.54
Mg#	77.4	83.0	76.0	80.9	81.4	75.8	75.4	75.7	74.5	74.1	75.4	78.1	76.2
P_{H2O} (MPa)	252	738	189	490	540	181	166	176	139	129	167	285	195
H_2O (wt%)		14.2		10.3	10.9								
σ_{H2O}		1.7		1.3	1.4								

Sample	17-05	17-05	17-05	17-05	17-05	17-05	17-05	17-05	17-05	17-05	17-04B	17-04B	17-04B
SiO_2	44.48	48.75	49.07	42.19	42.20	42.16	43.00	42.58	43.67	42.39	48.29	46.66	45.66
TiO_2	0.64	0.38	0.40	1.77	1.73	1.89	1.87	1.94	2.01	1.84	1.33	1.31	1.74
Al_2O_3	13.43	7.36	7.10	12.93	12.93	13.02	12.18	12.68	11.79	13.09	7.30	8.93	9.41
FeO	8.44	10.31	9.97	9.61	9.63	9.33	9.77	9.47	9.97	9.71	8.93	8.65	9.30
MnO	0.13	0.22	0.22	0.10	0.11	0.12	0.14	0.13	0.12	0.10	0.23	0.17	0.14
MgO	16.98	16.61	16.95	15.91	15.91	15.80	15.93	16.02	16.05	15.80	17.56	17.38	16.75
CaO	10.89	11.66	11.67	11.81	11.75	11.86	11.56	11.77	11.20	11.78	11.12	11.25	11.33
Na_2O	2.52	1.46	1.44	2.62	2.59	2.58	2.57	2.63	2.54	2.64	1.85	2.43	2.22
K_2O	0.36	0.27	0.32	0.34	0.33	0.31	0.31	0.32	0.30	0.33	0.29	0.34	0.42
P_2O_5	0.06	0.05	< 0.01	0.01	0.01	< 0.01	< 0.01	0.02	0.02	0.01	0.01	< 0.01	< 0.01
Cr_2O_3	0.02	0.50	0.46	< 0.01	0.04	< 0.01	0.02	0.01	0.04	0.03	0.01	0.01	0.03
NiO	0.04	< 0.03	< 0.03	< 0.03	0.04	< 0.03	< 0.03	0.03	< 0.03	< 0.02	0.02	0.02	0.03
Total	97.99	97.60	97.63	97.30	97.27	97.09	97.35	97.62	97.76	97.72	96.95	97.16	97.04
Mg#	78.2	74.2	75.2	74.7	74.6	75.1	74.4	75.1	74.1	74.4	77.8	78.3	76.2
P_{H2O} (MPa)	292	129	160	144	143	157	135	156	129	135	270	298	196
H_2O (wt%)													
σ_{H2O}													

Sample	17-04B	17-04B	17-04B	17-04B	17-04B	17-06A	17-06A	17-06A	17-06A	17-06A	17-06A	17-06A	17-06A
SiO_2	47.48	46.67	47.39	44.46	48.01	49.99	43.72	43.65	43.51	45.49	50.19	45.39	45.94
TiO_2	1.32	0.18	0.22	1.55	1.33	1.15	0.74	0.80	1.34	1.21	0.99	1.40	1.20
Al_2O_3	8.02	9.93	9.14	10.85	7.66	5.09	12.07	11.96	12.10	10.07	5.04	9.42	9.16
FeO	8.54	7.89	7.92	9.50	8.68	9.60	9.81	9.64	9.43	9.78	9.88	10.28	7.79
MnO	0.19	0.20	0.20	0.15	0.17	0.24	0.23	0.22	0.22	0.23	0.27	0.25	0.12
MgO	17.93	18.36	18.67	16.04	17.43	17.35	16.30	16.56	16.80	16.72	17.49	16.46	18.21
CaO	11.15	11.17	11.04	11.59	11.63	11.36	11.15	10.82	10.71	11.12	11.15	11.02	11.26
Na_2O	2.27	2.28	2.14	2.87	2.36	1.25	2.41	2.34	2.49	2.16	1.27	2.01	2.17
K_2O	0.32	0.40	0.31	0.48	0.35	0.21	0.41	0.35	0.33	0.37	0.20	0.37	0.15
P_2O_5	< 0.01	< 0.01	0.15	0.03	< 0.01	0.01	0.06	0.04	0.04	0.05	< 0.01	0.02	0.03
Cr_2O_3	< 0.01	0.02	< 0.01	< 0.01	0.03	0.01	< 0.01	< 0.01	< 0.01	0.01	0.02	0.10	0.03

Table 1 (continued)

Sample	17-04B	17-04B	17-04B	17-04B	17-04B	17-06A	17-06A	17-06A	17-06A	17-06A	17-06A	17-06A	17-06A
NiO	0.04	0.05	0.05	0.02	0.03	< 0.02	< 0.02	0.02	< 0.02	0.02	< 0.02	0.04	0.09
Total	97.25	97.17	97.22	97.55	97.67	96.26	96.91	96.38	96.97	97.22	96.51	96.75	96.05
Mg#	79.0	80.6	80.7	75.0	78.1	76.4	74.8	75.5	76.1	75.2	75.9	74.1	80.6
P_{H2O} (MPa)	339	465	480	154	286	203	147	170	192	161	185	126	470
H_2O (wt%)		10.0	10.2										10.2
σ_{H2O}		1.3	1.3										1.3

Sample	17-06A	17-06A	17-06A	17-06A	17-06A
SiO_2	47.65	46.62	47.30	46.67	49.31
TiO_2	1.16	1.34	1.25	1.43	1.20
Al_2O_3	8.94	9.34	9.07	9.37	5.76
FeO	7.12	8.34	7.61	8.55	10.18
MnO	0.09	0.12	0.12	0.11	0.27
MgO	18.52	17.52	18.30	17.61	17.22
CaO	11.57	11.52	11.51	11.15	11.34
Na_2O	2.12	2.11	2.12	2.28	1.37
K_2O	0.18	0.16	0.17	0.15	0.22
P_2O_5	0.03	0.01	0.03	0.01	0.01
Cr_2O_3	0.17	< 0.01	0.02	0.01	0.01
NiO	0.10	0.05	0.07	0.04	0.03
Total	97.65	97.14	97.56	97.40	96.93
Mg#	82.3	78.9	81.1	78.6	75.1
P_{H2O} (MPa)	638	337	511	315	156
H_2O (wt%)	12.6		10.7		
σ_{H2O}	1.5		1.3		

σ_{H2O} is an average of σ_+ and σ_-, the difference between water content calculated at $P \pm \sigma_{PH2O}$ (respectively) and the maximum water content of the equilibrium melt

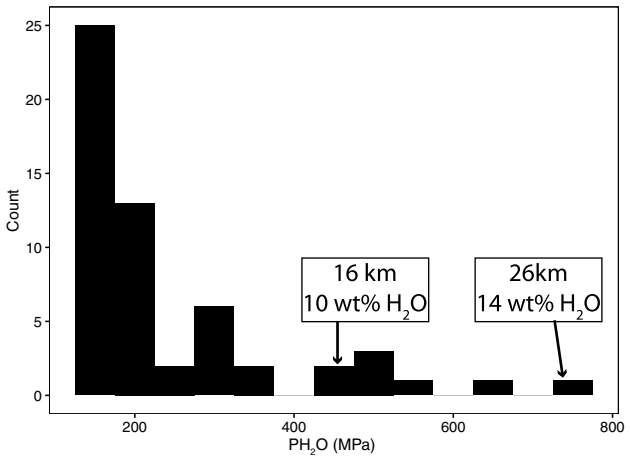

Fig. 10 Results from the Mg# geobarometer-hygrometer applied to amphibole analyses Mg# ≥ 74. We focus on results from the eight highest Mg# amphibole analyses (P_{H2O} > 400 MPa; highest and lowest extents are emphasized here by arrows) for our estimates of water content and minimum depth

enclaves from Shiveluch. The enclaves lack an equilibrium two oxide assemblage, so in our calculations, we assumed an oxygen fugacity of NNO + 2, reflecting the previously published estimates of oxygen fugacity of Shiveluch andesites (e.g., Humphreys et al. 2006). Calculated P_{H2O} ranged from 125–738 MPa (Fig. 10). Our assumption that the oxygen fugacity of a more evolved andesite is applicable to the oxygen fugacity of primitive melts is informed by studies showing that the oxygen fugacity of a melt does not appreciably change with differentiation (e.g., Kelley and Cottrell 2012; Brounce et al. 2014; Waters and Lange 2016), although melts may become oxidized by assimilation of crustal material or may become either more oxidized or reduced during significant degassing (especially of sulfur) in a shallow magma chamber (e.g., Mathez 1984; Holloway 2004; Kelley and Cottrell 2012; Humphreys et al. 2015; Waters and Lange 2016; Moussallam et al. 2016). Furthermore, the P_{H2O} calculated at NNO + 3 and NNO + 1 (one log unit above and below our estimate of NNO + 2, respectively) are within error of our original estimates except for the highest Mg# amphibole analysis, so the uncertainty in the oxygen

fugacity of the melt is relatively insignificant in our estimates of water content.

We focus the rest of our discussion on the highest Mg# amphibole analyses (all Mg# > 80) because, while amphiboles with lower Mg# can be crystallized from both deep super-hydrous and drier shallower melts, the highest Mg# amphiboles crystallized require the most liquidus depression, and thus inform our understanding of the most primitive, hydrous melts from which amphibole crystallized. The eight highest Mg# amphibole analyses give P_{H2O} from 464–738 MPa with an average of 551 MPa (Fig. 10). These values of P_{H2O} correspond to minimum pressures and depths of primitive amphibole crystallization because they reflect the minimum water content of magmas in equilibrium with these amphiboles. The results of the geobarometer-hygrometer applied to the eight highest Mg# amphibole analyses correspond to amphibole crystallization at depths of at least 16.4–25.8 km with an average of 18.9 km (depths calculated using the density from the anhydrous CIPW norm of Shiveluch andesite sample 7491 (2.8665 g/cm^3; Gorbach and Portnyagin 2011) and the results from the Mg# geobarometer-hygrometer in MPa, reported in Table 1). These results show that amphibole crystallization began within 10 km of the Moho (estimated to be at 30–40 km depth under Shiveluch; e.g., Iwasaki et al. 2013, and references therein) at deep crustal levels. The crystallization of amphibole in the lower crust is consistent with geochemical studies of suprasubduction zone ophiolites and geophysical studies of the continental crust, which both show evidence for early amphibole crystallization at arc settings (e.g., Bloomer et al. 1995; Parlak et al. 2000; Kocak et al. 2005; Bonev and Stampfli 2009; Jagoutz et al. 2011).

Although the amphiboles that we use to determine P_{H2O} are uniformly high in Mg#, they have a significant range in Al_2O_3 (> 10 wt% range for all high Mg# amphiboles and a ~ 7 wt% range among the amphiboles with Mg# > 80; Fig. 6, Table 1). The aluminum content of amphibole has been shown to be somewhat controlled by pressure; the pressure-dependent Al-Tschermak's exchange is the basis of the Al-in-hornblende barometer of Holland and Blundy (1994) for evolved melts and the empirical octahedrally coordinated aluminum barometers of Larocque and Canil (2010) and Krawczynski et al. (2012) for less evolved melts. However, a survey of amphiboles synthesized at relatively high pressure (i.e., > 450 MPa) shows that, although higher pressure experiments yield amphiboles with a maximum Al_2O_3 greater than those synthesized at lower pressures, Al_2O_3 in amphibole has a stronger correlation with melt Al_2O_3 than with pressure (Supplementary Fig. 10). The wide range in amphibole Al_2O_3 observed in our samples is thus likely attributable to crystallization from primitive melts with differences in Al_2O_3 caused by variability in the mineralogy of mantle sources (though some variability in amphibole Al_2O_3 may be attributable to polybaric crystallization). Seismic receiver function studies (e.g., Nikulin et al. 2010, 2012) and studies of xenoliths at this volcano (Bryant et al. 2007) suggest that primitive melts in this region are produced from at least two distinct mantle sources. The first is a hydrous, enriched pyroxenite source, also proposed by Pornyagin et al. (2007) to be a source of Shiveluch magma. This enriched mantle source is hypothesized to have been enriched by metasomatism during an earlier episode of subduction that produced the Sredinny Range (now, mostly extinct) volcanoes to the west of the CKD (Auer et al. 2009). Melts from this source would be relatively high in Al_2O_3 and would crystallize relatively aluminous amphiboles. The second source is a depleted peridotite mantle source characteristic of shallow subarc mantle. Partial melts of the depleted peridotite source would be less aluminous than the enriched pyroxenite and would be in equilibrium with amphiboles lower in Al_2O_3. Early mixing of these two endmember primitive melts may have produced melts with intermediate Al_2O_3, thus producing the full range of aluminum contents in high Mg# amphibole, but trace element analyses would be needed to confirm this hypothesis more definitively.

The results from the geobarometer-hygrometer can be translated to H_2O content of primitive melts using the H_2O solubility model of Papale et al. (2006). The model allows us to calculate H_2O solubility in melts accounting for magmatic temperature, pressure, and composition. There are several models of water solubility in basaltic melts (e.g., Dixon et al. 1995; Moore et al. 1998; Shishkina et al. 2010; Ghiorso and Gualda, 2015), but none that are experimentally calibrated above 500 MPa, mostly due to issues during quenching (e.g., Gavrilenko et al. 2019). We choose the Papale et al. (2006) model because its prediction of H_2O solubility at high pressures best agrees with the experimentally determined H_2O solubility in basaltic melts at 1 GPa (Mitchell et al. 2017). We use the P_{H2O} calculated for the eight highest Mg# amphibole analyses (Fig. 10) as magmatic pressure. This calculation yields the H_2O content of amphibole-crystallizing melts, assuming that the melt is saturated at the entered pressure (P_{H2O}). We reiterate that P_{H2O} may be less than the total pressure of crystallization (undersaturated), and that these melts also likely contain significant amounts of CO_2 (see discussion below). For the compositional parameter required for the Papale et al. (2006) model, we use the whole-rock composition of the enclave in which the amphibole was analyzed. We assume a temperature of 1100 °C (see next section for discussion). We find that the melts had water contents ranging from 10.0 ± 1.3 to 14.2 ± 1.7 wt% (Table 1).

P_{H2O} calculated from the amphibole Mg# geobarometer-hygrometer are minimum pressures of amphibole crystallization based on the amount of water needed to crystallize amphibole from a near-primary melt. Because CO_2 does not depress the liquidus temperature as much as water (Eggler

1976, 1978; Wyllie and Huang 1976a, b; Adam 1988), we do not consider it in our estimates of the water content inferred from the amphibole Mg# geobarometer-hygrometer, but it is an important volatile species at arc settings. Indirect estimates of CO_2 at arc settings suggest that there is at least 3000 ppm and up to 1.2 wt% CO_2 in arc magmas at depth (e.g., Wallace 2005; Shinohara et al. 2013; Plank and Manning 2019). In contrast, direct measurements of CO_2 from melt inclusions at arc settings have < 3000 ppm CO_2, due, in part, to the rarity of melt inclusions entrapped at lower crustal depths and, in part, to the technical difficulty of estimating CO_2 trapped in melt inclusion vapor bubbles or rehomogenizing and redissolving the CO_2 in the melt inclusion experimentally (e.g., Mironov et al. 2015; Moore et al. 2015; Wallace et al. 2015). Analyses of melt inclusions from Mount Etna in Italy (Kamenetsky et al. 2007), the Colima volcanic complex in Mexico (Vigouroux et al. 2008), Mount Saint Helens in Washington (USA) (Blundy et al. 2010), and Klyuchevskoy Volcano in Kamchatka (Mironov et al. 2015) corroborate the higher estimates from indirect methods.

We integrate CO_2 into our study by assuming that high Mg# amphiboles crystallized from a magma with a dissolved water content equivalent to P_{H2O} estimates from the amphibole Mg# geobarometer-hygrometer and with CO_2 contents of ~ 3800 ppm, equivalent to the amount of CO_2 analyzed in melt inclusions from Klyuchevskoy Volcano (Mironov et al. 2015). In the absence of measurements of CO_2 from Shiveluch melt inclusions, we take the measured CO_2 of Klyuchevskoy as an estimate for Shiveluch. Klyuchevskoy is an arc volcano in the CKD south of Shiveluch that is also thought to have particularly hydrous primitive magmas. By including 3800 ppm CO_2 with water contents equivalent to the P_{H2O} of the eight highest Mg# amphiboles analyzed, the minimum pressures of amphibole crystallization increase to 678–825 MPa (23.6–28.8 km depth; Fig. 11). The resulting range of water content in the volatile content (X_{H2O}) is 0.77–0.91, which is within reason based on estimates from Klyuchevskoy melt inclusions (Mironov et al. 2015).

Water is an incompatible element and thus, for water-undersaturated melts, any fractional crystallization will increase its concentration from parental melts. To calculate the water content of deeper parental melts in equilibrium with the mantle, the composition of enclaves is corrected for fractionation of primitive crystallizing phases olivine, amphibole, and clinopyroxene until the calculated

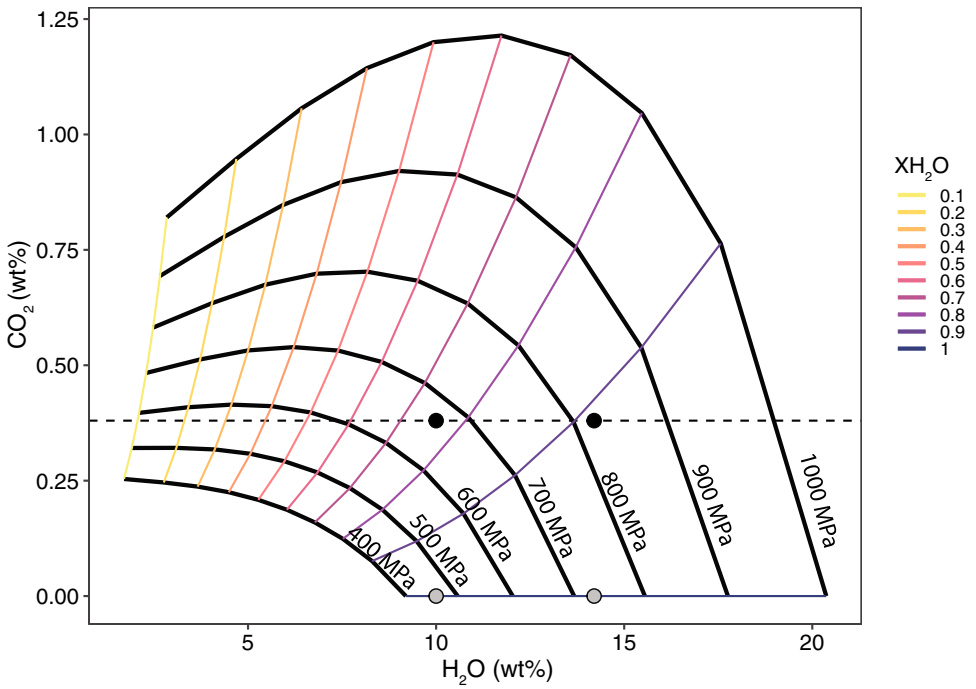

Fig. 11 H_2O and CO_2 solubility using the model of Papale et al. (2006) using the composition of enclave 17-06A and a temperature of 1100 °C at a variety of pressures (400–1000 MPa) and fluid compositions (XH_2O). Dashed line is at 3800 ppm CO_2, the estimated CO_2 content of Klyuchevskoy from melt inclusions (Mironov et al. 2015). Grey dots represent the range of estimated water content from P_{H2O} and black dots represent minimum pressure estimates of amphibole crystallization given a magma with water contents based on P_{H2O} and with 3800 ppm CO_2. The minimum pressure estimates (black dots) are at reasonable XH_2O based on Klyuchevskoy melt inclusions. Estimates of minimum pressures of crystallization at higher P_{H2O} are not as sensitive to CO_2 content as estimates at lower P_{H2O} because of the steep slope of the mixed volatile solubility model

composition is in equilibrium with Fo_{90} olivine. The H_2O contents are tracked during this calculation as components of the enclaves' initial compositions. The composition of olivine cores in enclaves with zoned olivine is mostly Fo_{90} (Fig. 3b), meaning that the parental melt was in equilibrium with olivine of approximately that composition. Fo_{90} also falls in the middle of the range of olivine magnesium number reported from ultramafic xenoliths collected at Shiveluch (Bryant et al. 2007), so Fo_{90} is representative of the mantle with which the Shiveluch parental melt was in equilibrium. We only corrected and used the compositions of enclaves with high forsterite olivine because they are higher in MgO than other enclaves, requiring the least amount of assumptions on what phases and what amounts are being crystallized. We corrected the compositions of enclaves by adding equilibrium composition olivine (Mg/Fe mineral-melt K_D of 0.32, appropriate based on the NBO/T [nonbridging oxygen (NBO) per tetrahedrally coordinated cation (T)] of hydrous, primitive arc melts [~ 1.5; Kushiro and Mysen 2002]), equilibrium composition clinopyroxene (Mg/Fe mineral-melt K_D of 0.27; Putirka 2008), and a static composition of amphibole back to whole-rock compositions in 1 wt% total increments. The composition of amphibole that was added back was the second highest Mg# amphibole we analyzed (Mg# = 82.3). We chose this amphibole composition because it is the highest Mg# amphibole closest to the median Al_2O_3 content of high Mg# amphiboles (8.94 wt% Al_2O_3; Fig. 6). The ratio of olivine, clinopyroxene, and amphibole added to the enclave compositions was adjusted until the corrected compositions were comparable to the compositions of the 3959 and 8363 BP basaltic to basaltic andesitic tephra, which we hypothesize are petrogenetically related to more evolved magmas at Shiveluch; care was taken to match the calcium content of the corrected compositions to that of the tephra (~ 8 wt%) since the calcium content cannot be reproduced by olivine addition alone and is sensitive to the ratio of clinopyroxene to amphibole added to the enclave compositions. A 6:3:1 ratio of olivine to clinopyroxene to amphibole added back to enclave compositions satisfies our requirements, with 14.9–23.2 total percent crystals added back to enclave compositions (Supplementary Table 8).

We calculated the water content of deep parental melts using the two enclaves that contained both high forsterite olivine and analyses of one or more of the eight highest Mg# amphiboles (samples 17-02B and 17-04 K). Enclave 17-02B contained two very high Mg# analyses of amphibole, so we used the highest magnesium amphibole in our calculation. Based on this calculation, the melts in equilibrium with Fo_{90} (parental melts in equilibrium with the mantle) had water contents ranging from 8.9 to 10.8 wt%.

Uncertainty in water content (σ_{H2O}) ranges from 1.3–1.7 wt%. Uncertainty was estimated by calculating H_2O solubility using the Papale et al. (2006) equation at $P_{H2O} \pm 93$ MPa (the uncertainty associated with the geobarometer-hygrometer). Because the Papale et al. (2006) solubility model is nonlinear, our errors are asymmetric, but the asymmetry (using the mathematical definition given in Barlow, 2006) is low compared to the total uncertainty (no greater than 0.07), so we approximate the errors as symmetric. The quoted uncertainties in Table 1 are the average of σ_+ and σ_- for each point.

Pressure

We calculated the minimum pressures required for generating the primitive enclave magma compositions using the thermobarometer of Lee et al. (2009). The model calculates minimum depths of multiple saturation with mantle olivine and orthopyroxene and magmatic temperature using the primitive magma's composition (especially its MgO, SiO_2, and H_2O content). We used the compositions of enclaves corrected to be in equilibrium with Fo_{90} by addition of olivine, clinopyroxene, and amphibole described in the previous section as inputs to the thermobarometer. For these calculations, we assumed a Fe^{3+}/Fe_{total} of 0.32, which is the calculated Fe^{3+}/Fe_{total} using the equations in Kress and Carmichael (1991) at NNO + 2. The calculations were performed assuming 9–16.7 wt% added water. Temperatures calculated from the Lee et al. (2009) thermobarometer overlap with the uncertainty of our estimates of magmatic temperatures from Al-in-olivine thermometry for water contents ≥ 14 wt%. Temperatures approaching the average temperature from independent Al-in-olivine thermometry methods (1062 °C) are only calculated by the Lee et al. (2009)

Table 2 Calculated pressure and temperature from Lee et al. (2009) thermobarometer for the compositions of enclaves corrected to be in equilibrium with Fo_{90}

	9 wt% H_2O		10.7 wt% H_2O		13.8 wt% H_2O		16.7 wt% H_2O	
	T (°C)	P (GPa)	T (°C)	P (GPa)	T (°C)	P (GPa)	T (°C)	P (GPa)
17-04K	1146	1.1	1128	1.1	1099	1.2	1078	1.3
17-05	1190	1.5	1167	1.5	1130	1.6	1103	1.7
17-09A	1169	1.3	1149	1.3	1115	1.4	1090	1.5
17-02B	1162	1.2	1142	1.3	1109	1.3	1085	1.4
17-04F	1148	1.1	1130	1.1	1100	1.2	1078	1.3

thermometer at water contents greater than or equal to 16.7 wt% H_2O, consistent with the fact that water contents calculated from amphibole Mg# hygrometry must be minima. The minimum depths of primitive magma equilibration with the mantle ranged from 1.1–1.7 GPa (2σ uncertainty is 0.2 GPa); higher water content magmas had higher calculated pressures (Table 2). This range of pressure corresponds to depths of 36.7–56.8 km, calculated assuming a simple lithospheric column of 2/3 andesite and 1/3 harzburgite with a total density of 2.9947 g/cm^3. That density was calculated from the density from the anhydrous CIPW norm of andesite used to calculate depth in the previous section and from the density from the anhydrous CIPW norm of harzburgite sample SHX-03-01 erupted at Shiveluch reported in Bryant et al. (2007). This range in depth overlaps with the deeper limits of estimates of the seismologic Moho depth under Shiveluch (30–40 km; e.g., Iwasaki et al. 2013, and references therein). The overlap of Moho depth and calculated depth suggests that the calculated depths reflect minimum depths of multiple saturation with olivine and orthopyroxene, rather than average pressures of partial melting.

Evidence for Co-crystallization of high Mg# amphibole and olivine support quantitative evidence for very high magmatic water contents

Maximum estimates of water contents from melt inclusion analyses (e.g., Humphreys et al. 2008; Tolstykh et al. 2015) and a Ca-in-olivine geohygrometer (Gavrilenko et al. 2016a) range from 5.1 to 7.2 wt% H_2O in Shiveluch basalts and andesites. These melt inclusion analyses are from plagioclase-hosted inclusions and are useful for determining the minimum water content of the host andesite, but they do not record the water content of mid to lower crustal primitive magmas. The Ca-in-olivine geohygrometer applied to primitive basaltic melts, however, estimates 6.4 wt% H_2O (Gavrilenko et al. 2016a). In this section, we support our quantitative estimates for a deep, superhydrous (10–14 wt% H_2O) primitive melt with evidence of early amphibole crystallization.

High magnesium (i.e., Mg# > 74) pargasitic amphibole inclusions in high forsterite (i.e., Fo > 90) olivine are evidence that amphibole joined olivine as a liquidus phase and the two co-crystallized from a primitive, magnesian melt. Experimental studies of the liquid line of descent of hydrous basalts show that early co-precipitation of amphibole and olivine requires magma with at least 8 wt% H_2O (e.g., Helz 1973). In addition, experimental studies of Mount Shasta, CA, another superhydrous eruptive center, showed that comparably high-magnesium amphibole co-crystallized with high-Fo olivine at water contents of up to 14 wt% at lower-crustal temperatures and pressures (Krawczynski et al. 2012). The preservation of amphibole in olivine grains at Shiveluch suggests a magma of similar hydrous nature.

Table 3 Starting, amphibole, and plagioclase compositions used in fractional crystallization models

	Starting compositions		Amphibole				Plagioclase
	3959-year-old tephra	8363-year-old tephra	High Mg	Lower Mg	Co-crystallized with Fo_{80}	Lowest Mg	Groundmass Core
			Sample 05	Sample 04K	Sample 04D	Sample 04B	Sample 06A
SiO_2	53.17	54.12	44.48	42.11	46.43	42.77	48.19
TiO_2	0.82	0.74	0.64	2.29	1.19	2.00	0.02
Al_2O_3	13.40	15.64	13.42	12.73	8.28	12.20	32.67
FeO	8.85	7.52	8.44	10.85	10.52	11.89	0.39
MnO	0.16	0.14	0.13	0.13	0.24	0.20	0.0
MgO	13.85	9.51	16.98	14.83	16.42	13.70	0.0
CaO	8.20	7.99	10.89	11.33	11.24	11.24	15.08
Na_2O	2.65	3.23	2.52	3.26	2.32	2.37	2.83
K_2O	1.56	0.92	0.36	0.26	0.36	0.49	0.04
P_2O_5	0	0.17	0.06	0.01	< 0.01	0.03	0.02
Cr_2O_3	–	–	0.02	0.02	0.03	< 0.01	0.11
NiO	–	–	0.06	0.06	< 0.02	< 0.02	0.02
Total	100	100	98.0	97.9	97.0	97.1	99.23
Mg#	69	69	78.2	70.9	73.6	67.2	–
An	–	–	–	–	–	–	74.5

Tephra compositions are from Ponomareva et al. (2007a)

Table 4 Conditions for models shown in Fig. 12

Starting composition	3959-year-old tephra									8363-year-old tephra								
Model type	Ol + Cpx + Plag			Ol + Amph + Plag				Ol + Cpx + Amph + Plag				Ol + Cpx + Plag			Ol + Amph + Plag			Ol + Cpx + Amph + Plag			
Stage no	1	2	3	1	2	3	4	1	2	3	4	1	2	3	1	2	3	4	1	2	3	4
X_{ol}	0.8	0.3	0.05	0.8	0.3	0.3	0.05	0.8	0.3	0.3	0.05	0.5	0.3	0.05	0.5	0.3	0.3	0.05	0.5	0.3	0.3	0.05
X_{cpx}	0.2	0.7	0.9	0	0	0	0	0	0	0.1	0.2	0.5	0.7	0.9	0	0	0	0	0	0	0.1	0.2
X_{amph1}	0	0	0	0.2	0	0	0	0.2	0	0	0	0	0	0	0.5	0	0	0	0.5	0	0	0
X_{amph2}	0	0	0	0	0.7	0	0	0	0.7	0	0	0	0	0	0	0.7	0	0	0	0.7	0	0
X_{amph3}	0	0	0	0	0	0.7	0	0	0	0.6	0	0	0	0	0	0	0.7	0	0	0	0.6	0
X_{amph4}	0	0	0	0	0	0	0.9	0	0	0	0.7	0	0	0	0	0	0	0.9	0	0	0	0.7
X_{plag}	0	0	0.05	0	0	0	0.05	0	0	0	0.05	0	0	0.05	0	0	0	0.05	0	0	0	0.05
No. Steps	6	18	26	6	7	11	26	6	7	11	26	6	19	11	6	10	9	11	6	10	9	11
Cumulative X_{amph}	0	0	0	1.2	5.7	12.1	28.4	1.2	5.7	11.7	23.9	0	0	0	2.9	9.2	14.4	21.7	2.9	9.2	13.6	19.3

"Amph 1" is the high Al, high Mg amphibole composition; "Amph 2" is the lower Mg amphibole composition; "Amph 3" co-crystallized with Fo_{80} olivine; and "Amph 4" is the lowest Mg composition and co-crystallized with plagioclase. Each "stage" of the model corresponds to a different fractionating assemblage or to a different proportion of phases being fractionated. The cumulative amount of amphibole fractionated throughout the model is calculated by multiplying the proportion of amphibole by the number of 1 wt% fractionation steps and adding the amount of amphibole fractionated in the last step

Fractional crystallization of amphibole-bearing assemblages relates enclaves and andesites at Shiveluch volcano

Decreasing trends in whole-rock CaO and TiO_2 and increasing Al_2O_3 with decreasing MgO (Fig. 7) defined by the compositions of enclaves and andesites can only be reproduced by fractionation of amphibole-bearing assemblages from the melt. Feasibly, crystallization and fractionation of Ti-bearing oxides and clinopyroxene could also replicate these trends. However, there is no petrographic evidence for early crystallization of titanium-rich oxides from the magnesian melts at Shiveluch, and such Ti-rich oxides would not be expected to crystallize from hydrous melts with such high MgO (i.e., > 7wt%; e.g., Sisson and Grove 1993). Magnesian clinopyroxene in coexistence with high forsterite olivine in the enclaves and in cumulate samples is evidence that clinopyroxene was an early crystallizing (and potentially fractionating) phase. However, the clinopyroxene in these samples is too low in TiO_2 (Supplementary Table 5) for its fractionation to cause the observed decrease in TiO_2 in the enclaves and andesites. In the absence of Ti-bearing oxides, amphibole is the dominant Ti-bearing phase; its fractionation is essential to drive the decrease in TiO_2 with decreasing MgO. Thus, although clinopyroxene may have been fractionated from the melt, trends in TiO_2 with decreasing MgO require that amphibole was an abundant fractionating phase. The fractionation of amphibole from magnesian melts is also consistent with the petrologic evidence of the phase's co-crystallization with magnesian olivine, as discussed in the previous section. Increasing Al_2O_3 and Sr of the basaltic andesite enclaves as a function of MgO and the lack of a europium anomaly in these samples suggests that plagioclase was not a significant fractionating phase from the melt. As MgO decreases, Al_2O_3 and Sr increase monotonically in the enclaves; if plagioclase had been a significant fractionating phase, both elements in the melt would have decreased. Additionally, had plagioclase been a significant fractionating phase, enclaves would have a notable Eu anomaly, which they do not. The lack of plagioclase fractionation may be due to its suppression due to high water contents, as has been observed experimentally (e.g., Yoder and Tilley 1962; Sisson and Grove 1993; Danyushevsky 2001; Parman et al. 2011; Grove et al. 2012; Krawczynski et al. 2012).

To quantitatively determine the amount of fractional crystallization needed to relate enclaves and andesites, we made models of liquid lines of descent starting from the compositions of the 8363 and 3959 BP tephra units that are the most magnesian magmas erupted from Shiveluch (Mg# 69 for both tephras; Table 3). The dominant phenocryst assemblage in the tephra informed our choice of

fractionating phases in our model. In all models, solids in equilibrium with the melt are fractionated in 1 wt% steps.

Olivine is a dominant phenocryst phase in the tephra (up to 10 vol%) with compositions ranging up to Fo_{93} (Volynets 1997). Our enclaves also contain olivine in a continuous range from Fo_{74} to Fo_{92}. The range of olivine composition in the enclaves suggests that the phase was continuously crystallizing from an evolving melt. In our model, equilibrium olivine compositions were calculated and fractionated from the melt using a fixed K_D of 0.32 (Kushiro and Mysen 2002). In our models, the proportion of olivine being fractionated from the melt relative to other phases decreased with progressive crystallization steps, reflecting the relatively low abundance of olivine in andesites erupted at Shiveluch (e.g., Gorbach et al. 2016).

Clinopyroxene was included in our model because it is a phenocryst phase in the tephra (e.g., Volynets 1997) and in the enclaves. In our models, we adjusted the clinopyroxene composition using a fixed K_D^{Mg-Fe} of 0.27 (Putirka 2008). We used a clinopyroxene composition that did not include any minor elements such as Al_2O_3, MnO, TiO_2, or Na_2O for simplicity, but note that the titanium content of natural clinopyroxene in the enclaves is low relative to amphibole in these rocks (Supplementary Table 5). For models fractionating clinopyroxene from the melt, clinopyroxene fractionation began when the melt approached the Mg/Fe ratio in equilibrium with the Mg/Fe ratio of the most magnesian clinopyroxene compositions analyzed in the enclaves, and the relative proportion of clinopyroxene fractionated increased as the model progressed.

Amphibole is the final major phenocryst phase included in our model. It is also a major phase in the tephra (up to 20 vol%; Volynets 1997). We chose to fractionate compositions of actual amphiboles from the enclaves because of the lack of a good predictive model for amphibole compositions and the compositional complexity of amphibole. We fractionated four different compositions of amphibole throughout the model (Tables 3, 4) that represent the gamut of amphibole compositions in Mg# and Al_2O_3 in the enclaves (as represented in Fig. 6). Overall, we utilized the petrographic context of amphiboles to infer their crystallization sequence, which is consistent with generally decreasing Mg# as crystallization progresses.

The first composition of amphibole fractionated from the melt is in equilibrium with high forsterite (Fo_{90}) olivine and was analyzed in the most magnesian enclave we sampled (17-05). This first fractionating amphibole is high in both Mg# (Mg# 78; Table 3) and Al_2O_3 consistent with crystallization starting at the depth required for water solubility to be high enough to co-crystallize high magnesium olivine and amphibole (e.g., Krawczynski et al. 2012). The second amphibole composition is from the core of a normally zoned groundmass amphibole in a glassy enclave that contained high forsterite (i.e., Fo ≥ 88) olivine (17-04 K). It is lower in Mg# (Mg# 71) and Al_2O_3 than the first fractionating amphibole and is higher in TiO_2. The third amphibole composition fractionated in the model is from an amphibole rim around a low forsterite (i.e., Fo_{80}) olivine with a symplectite reaction rim. The textural relationship with low forsterite olivine suggests crystallization from a more evolved melt. The third amphibole composition is lower in TiO_2 than the second amphibole composition, which could be an effect of locally low TiO_2 due to the crystallization of iron oxides in the nearby olivine symplectite rim. Finally, the last composition of amphibole that is fractionated in the model is lowest in Mg# (Mg# 67), reflecting its crystallization from an even more evolved melt. Inclusions of plagioclase in amphibole show that amphibole similar in composition to our final fractionating composition is in equilibrium with high An (i.e., ~An_{74}) plagioclase, which reflects crystallization from a melt similar to the host andesite in composition and likely similar H_2O contents of 7 wt% (e.g., Humphreys et al. 2008).

We also used the enclaves' dysprosium anomaly (Dy/Dy^*) to estimate the amount of amphibole fractionated from primitive melts independently from the enclaves' major element compositions. We assume that a bulk rock $Dy/Dy^* < 1$ is generated by the fractionation of amphibole from a melt and that the parental melt initially has $Dy/Dy^* = 1$. Amphibole has a $Dy/Dy^* > 1$ because it is enriched in MREE relative to other REE. We calculated a representative Dy/Dy^* of amphibole in our samples using the whole rock La, Yb, and Dy and mineral proportions of cumulate sample 17-04L and mineral-melt partition coefficients of La, Yb, and Dy for amphibole, plagioclase, clinopyroxene, and apatite (the partition coefficients used for amphibole, plagioclase, and clinopyroxene are identical to the partition coefficients used by Davidson et al. (2013) in their formulation of the dysprosium anomaly from Fujimaki et al. (1984), Johnson (1994), Botazzi et al. (1999); the partition coefficients for La and Dy for apatite are from the experimental study of Watson and Green (1981) and the apatite-melt partition coefficient for Yb was determined from natural samples by Paster et al. (1974)) and found that the amphibole Dy/Dy^* was 1.52, higher than the bulk rock Dy/Dy^* of 1.27 of sample 17-04L (Electronic Supplementary Material).

$$Dy/Dy^*_{\text{sample}} = Dy/Dy^*_i - Dy/Dy^*_{17-04\text{L}}\left(X_{\text{amph}}\right),$$

where Dy/Dy^*_i is equal to 1 to calculate X_{amph}, the proportion of amphibole fractionated from the melt with a given Dy/Dy^*, in all of our samples. We found the uncertainty in Dy/Dy^* by propagating error from ICP-MS analysis of La_N, Yb_N, and Dy_N (5% of their value) through the calculation of Dy/Dy^*. The samples range in calculated X_{amph}

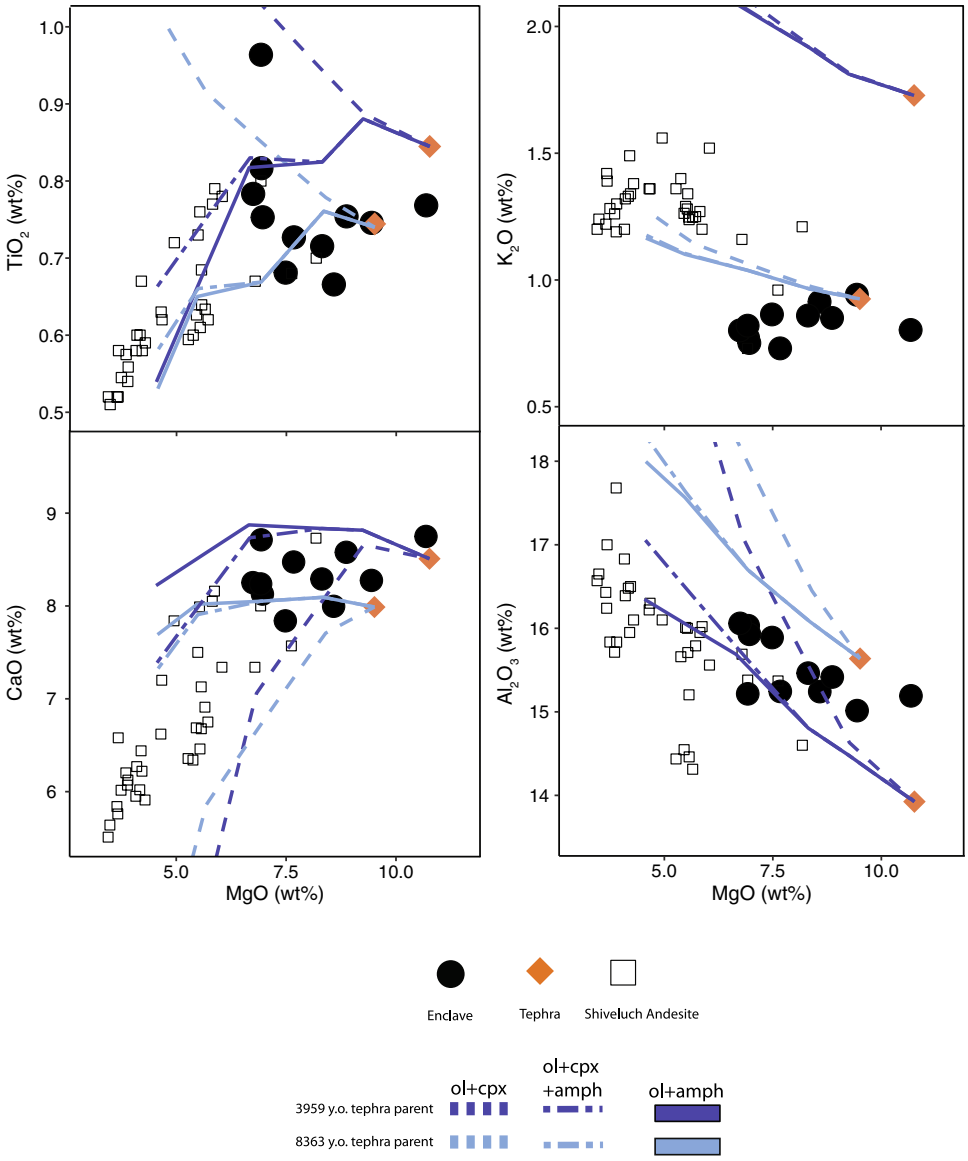

Fig. 12 Results of fractional crystallization modeling. Orange diamonds are 3959 and 8363-year-old tephra compositions from Ponomareva et al. (2007a). Lines are modeled liquid lines of descent from the 3959 and 8363-year-old tephra. Dark blue lines are models from the 3959-year-old tephra parent starting composition and light blue lines are models from the 8363-year-old tephra starting composition. Solid blue lines are models that fractionate amphibole, olivine, and plagioclase. Double dashed lines are models that fractionate olivine, clinopyroxene, amphibole, and plagioclase. Finally, dashed lines are models that fractionate olivine, clinopyroxene, and plagioclase (amphibole absent). Only amphibole-present models reproduce the trends defined by natural samples. For results of models for other major elements, the reader is directed to Supplementary Fig. 11. Proportions of mineral phases fractionated to produce these models is given in Table 4

from 0 (sample 17-05) to 0.08 (sample 17-04D). Considering the uncertainty in Dy/Dy*, the maximum percent of amphibole fractionated from a primitive melt to generate an enclave melt composition is ~ 13%. Using this calculation, the one published ICP-MS analysis of andesite from Shiveluch (Davidson et al. 2013) would have had 19% amphibole fractionation.

In our model, we also fractionated minor amounts of plagioclase as the calculated residual melt composition approached the MgO content of most published analyses of andesite because plagioclase has been found to be in equilibrium with Shiveluch andesitic melts and is abundant in the mafic enclaves (e.g., Humphreys et al. 2006). Early fractionating plagioclase is not considered in these models because it would decrease the aluminum content of the residual liquid with differentiation, which is inconsistent with the trend defined by mafic enclaves and andesites at Shiveluch (Al_2O_3 increases with decreasing MgO; Fig. 7). Furthermore, the high inferred H_2O content suppresses plagioclase crystallization. For simplicity, the plagioclase composition fractionated in the model was held constant. The composition was a representative analysis of the calcium-rich core of groundmass plagioclase in enclave 17-06A (An_{74}; Table 3). Orthopyroxene and accessory Ti-bearing oxide phases were not included in this model because they are volumetrically insignificant (i.e., $<<1\%$) in the enclave samples themselves.

Only amphibole-present models satisfactorily reproduce the trends defined by enclaves and andesites. Our models, while quantitative in nature, are not meant to represent a unique liquid line of descent that is followed by Shiveluch magmas. Instead, the models shown in Fig. 12 and

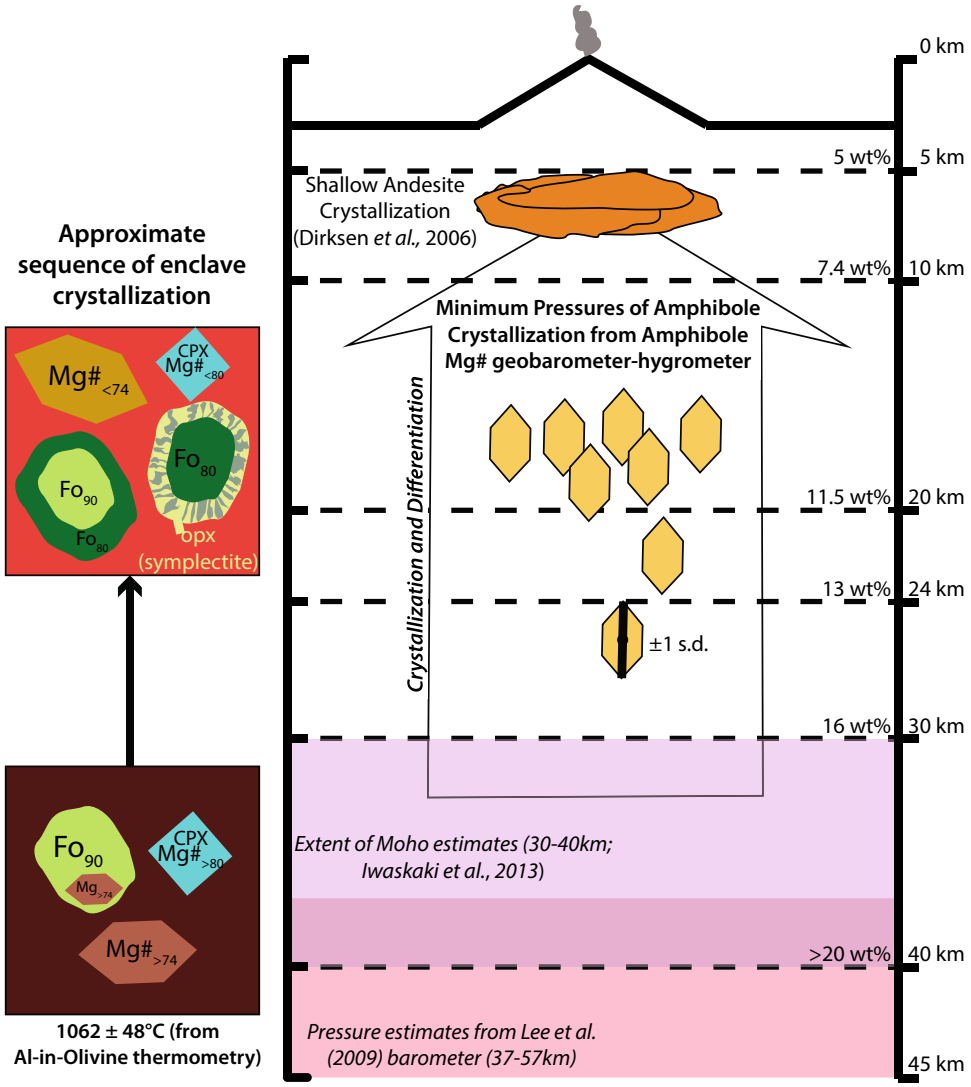

Fig. 13 Model of Shiveluch plumbing system and sequence of crystallization. Water contents on y-axis are water solubility in a basaltic melt from Papale et al. (2006) in a CO_2-free system. Constraints on the shallow magma storage region are from Dirksen et al. (2006). Purple box represents a range of Moho estimates in this region (30–40 km) from Iwasaki et al. (2013). Pink box represents the upper range of pressure estimates from the Lee et al. (2009) barometer, which extend beyond the scale of this diagram (37–57 km). Yellow amphiboles represent the results from the application of the Mg# geobarometer-hygrometer to the eight highest Mg# amphibole analyses ± 93 MPa, and show minimum depths of amphibole crystallization, assuming a CO_2-free system. Including 3800 ppm CO_2, the range of minimum depths of amphibole crystallization is shifted deeper to 24–29.5 km but are not pictured here. Approximate sequence of crystallization shows the effects of magmatic differentiation on crystal chemistry. The first amphiboles to crystallize at depth will have high Mg#, but variable Al_2O_3. These high Mg# amphiboles are in equilibrium with high forsterite olivine and magnesian clinopyroxene. Because of their high dissolved water contents, magmas in equilibrium with high Mg# olivine, amphibole, and clinopyroxene are relatively low-temperature; the average temperature from the application of the aluminum in olivine thermometer to relatively magnesian olivines in the enclaves is 1062 ± 48 °C. We show symplectite-rimmed olivine in the more evolved assemblage because they are present in the enclaves, but we do not constrain the cause or timing of the symplectite-forming reaction, which may occur in more primitive melts

Supplementary Fig. 11 compositionally bracket the enclave and andesite compositions. The exact composition of any given enclave or andesite could be reproduced by crystallizing the melts at different P, T, f_{H2O}, thus altering the proportions and chemistry of minerals being fractionated from the melt. Our models also show that the early fractionation of amphibole is necessary to approximate enclave and andesite bulk compositions. In our models, 0.2–12% amphibole is fractionated to reproduce the full range of enclave compositions (Table 4). The range of amphibole fractionated in our model agrees with the 0–13% amphibole fractionation independently calculated using the dysprosium anomaly.

Interestingly, none of our models predict the K_2O contents of enclaves and andesites. The potassium content of enclaves seems to decrease even from the lowest potassium starting composition (the 8363-year-old tephra). Two possibilities might explain this observation. The first is that neither tephra composition is representative of the true parental magma to the enclaves. Although our models compositionally bound the enclaves in most variation diagrams, they do not exactly reproduce the compositions of all of the enclaves. A parental melt lower in calcium, titanium, and potassium and higher in aluminum than the tephra compositions but yet unsampled might better reproduce the compositions of the enclaves. Another possibility is that late-stage fluid loss (i.e., volatile-induced differentiation; e.g., Ferlito and Lanzafame 2010) from the enclaves decreased their bulk K_2O. At lower pressures, the enclave melts would be water-saturated and begin to degas. The degassed fluid would leach fluid mobile elements like potassium, thereby decreasing its concentration in the melt. Rubidium, another fluid-mobile element, shows similar behavior as K_2O as MgO decreases (Supplementary Fig. 7).

We also evaluated the hypothesis that the whole rock major element geochemical trends defined by enclaves and andesites could be explained by mixing processes. One suggestion is that mixing andesite melt with primitive basaltic melts can reproduce the gamut of enclaves intermediate in composition between the two mixing endmembers (e.g., Bacon 1986; Eichelberger et al. 2000, 2006; Plail et al. 2014, 2018). Rare earth element abundances of enclaves and andesites support fractionation rather than mixing as the dominant process producing the intermediate melts. Enclaves with major element compositions between the most magnesian enclave analyzed (sample 17-05, against which REE are normalized in Fig. 8b) and Shiveluch andesites ("intermediate" enclaves) have higher REE abundances than the more magnesian enclaves. Shiveluch andesite has lower MREE and HREE abundances than these "intermediate" enclaves (Fig. 8a, b). Mixing of andesite and very magnesian enclaves could thus not produce relatively higher MREE and HREE abundances of the "intermediate" enclaves. The increasing abundance in most REE from more to less magnesian enclaves can be easily explained with fractional crystallization. The rare earth elements are generally incompatible, so their relative abundance is increased with melt differentiation. The deficit of MREE in the andesite can be explained by fractional crystallization of amphibole. Although mixing could feasibly explain the major element compositions of enclaves, it is incapable of explaining their rare earth element compositions.

While the whole-rock composition of enclaves and andesites suggests that mixing is not the dominant process in their generation, petrologic evidence in the enclaves suggests that some open system mixing did occur. For example, low Mg# amphibole cores with low-An plagioclase and apatite inclusions were inherited from a more evolved source saturated in apatite; based on trends in whole-rock P_2O_5, the source had at most 5 wt% MgO. Similarly, larger sodic and oscillatory zoned plagioclase crystals in the enclaves were inherited from a more evolved source, either by crustal assimilation or by mixing with a more evolved crystalline mush in a shallow crustal chamber. Differentiating between the effects of crustal assimilation and other open system processes would require isotopic analyses of these samples, and is beyond the scope of this study.

Conclusions

Our model for the formation of the Shiveluch enclaves is summarized in Fig. 13 and involves the differentiation of a primitive, superhydrous magma to produce the erupted andesites at Shiveluch. Primitive magmas had water contents of 8.9 to 10.8 wt% H_2O and temperatures of 1062 ± 48 °C. The melt crystallized high Mg# olivine, amphibole, and clinopyroxene, increasing the water content to 10–14 wt%. Our estimates for the water content of these primitive melts are the highest ever found. Ultimately, fractionation of these phases from the melt produced the andesite that was stored in a shallow magma chamber at a temperature of ~ 860 °C and pressures of ~ 160–180 MPa (Dirksen et al. 2006). The andesite was in equilibrium with amphibole and plagioclase. Recharge of the andesite with primitive magmas generated the enclaves.

This study extends the model of the magma plumbing system under this volcano to a greater depth. It shows that the andesitic liquid can be produced by fractional crystallization. Our proposal that amphibole and olivine were major, early crystallizing and fractionating phases are comparable to proposed liquid lines of descent for other very hydrous arc volcanoes such as Mount Shasta in the Cascades (e.g., Grove et al. 2012). Ultimately, this study shows that careful petrographic analysis of mafic enclaves can expand our understanding of deep magmatic processes including differentiation and recharge in arc systems.

Acknowledgements The authors acknowledge support from Washington University in Saint Louis for funding field and lab work associated with this project. AEG and MG acknowledge the McDonnell Center for the Space Sciences for funding. PR acknowledges support from National Science Foundation EAR Grants #1426820 and #1719687. Fieldwork for NVG was supported by Grant #15-05-06440 from the Russian Foundation for Basic Research. MJK acknowledges support from National Science Foundation EAR Grant #1654683. We thank Paul Carpenter for help with electron probe microanalysis. This manuscript benefitted from helpful conversations with Rita Parai, Doug Wiens, David Fike, and Kelsey Prissel. M. Portnyagin and P. Ulmer are

thanked for their helpful reviews of this manuscript, and O. Müntener is thanked for editorial handling and review.

Funding Funding from Washington University in Saint Louis is acknowledged for completion of this project. AEG and MG also acknowledge the McDonnell Center for Space Sciences for funding. MJK acknowledges support from NSF EAR Grant #1654683. Fieldwork for NVG was supported by Grant #15-05-06440 from the Russian Foundation for Basic Research. PR acknowledges support from NSF EAR Grants #1426820 and #1719687.

Code availability Matlab codes used for quantitative fractionation modeling and compositional correction of enclaves is available on request.

Compliance with ethical standards

Conflict of interest We do not have any conflict of interest to declare.

References

Adam J (1988) Dry, hydrous, and CO_2-bearing liquidus phase relationships in the CMAS system at 28 Kb and their bearing on the origin of alkali basalts. J Geol 96(6):709–719

Alonso-Perez R, Muntener O, Ulmer P (2008) Igneous garnet and amphibole fractionation in the roots of island arcs: experimental constraints on andesitic liquids. Contrib Mineral Petrol 157:541–558

Armstrong JT, Donovan JJ, Carpenter PC (2013) CALCZAF, TRYZAF and CITZAF: the use of multi-correction-algorithm programs for estimating uncertainties and improving quantitative X-ray analysis of difficult specimens. Microsc Microanal 19(Suppl 2):812–813

Asafov EV, Sobolev AV, Gurenko AA et al (2018) Belingwe komatiites (2.7 Ga) originate from a plume with moderate water content, as inferred from inclusions in olivine. Chem Geol 478:39–59

Auer S, Bindeman I, Wallace P, Ponomareva V, Portnyagin M (2009) The origin of hydrous, high-d^{18}O voluminous volcanism: diverse oxygen isotope values and high magmatic water contents within the volcanic record of Klyuchevskoy volcano, Kamchatka, Russia. Contrib Mineral Petrol 157:209

Bacon CR (1986) Magmatic inclusions in silicic and intermediate volcanic rocks. J Geophys Res 91(B6):6091–6112

Baker MB, Grove TL, Price R (1994) Primitive basalts and andesites from the Mt. Shasta region, N. California: products of varying melt fraction and water content. Contrib Mineral Petrol 118(2):111–129

Barlow R (2006) Asymmetric statistical errors: statistical problems in particle physics. Astrophys Cosmol 56–59

Batanova VG, Sobolev AV, Kuzmin DV (2015) Trace element analysis of olivine: high precision analytical method for JEOL JXA-8230 electron probe microanalyser. Chem Geol 419:149–157

Belousov A, Belousova M, Voight B (1999) Multiple edifice failures, debris avalanches and associated eruptions in the Holocene history of Shiveluch volcano, Kamchatka, Russia. Bull Volcanol 61:324–342

Bird P (2003) An updated digital model of plate boundaries. Geochem Geophys Geosyst 4:3

Blatter DL, Carmichael ISE (2000) Hydrous phase equilibria of a Mexican high-silica andesite: a candidate for a mantle origin? Geochim Cosmochim Acta 65(21):4043–4065

Blatter DL, Sisson TW, Hankins B (2017) Voluminous arc dacites as amphibole reaction-boundary liquids. Contrib Mineral Petrol 172:27

Bloomer SH, Taylor B, Macleod CJ, Stern RJ, Fryer P, Hawkins JW, Johnson L (1995) Early arc volcanism and the ophiolite problem: a perspective from drilling in the Western Pacific. In: Taylor B, Natland J (eds) Active margins and marginal basins of the Western Pacific. American Geophysical Union Geophysical Monograph, Washington DC, vol. 88, pp. 1–26

Blundy J, Cashman KV, Rust A, Witham F (2010) A case for CO_2-rich arc magmas. Earth Planet Sci Lett 290(3–4):289–301

Bonev N, Stampfli G (2009) Gabbro, plagiogranite and associated dykes in the supra-subduction zone Evros Ophiolites, NE Greece. Geol Mag 146(1):72–91

Botazzi P, Tiepolo M, Vanucci R, Zanetti A, Brumm R, Foley SF, Oberti R (1999) Distinct site preferences for heavy and light REE in amphibole and the prediction of $^{Amph/L}D_{REE}$. Contrib Mineral Petrol 137:36–45

Brounce MN, Kelley KA, Cottrell E (2014) Variations in Fe^{3+} / Fe_{total} of mariana Arc basalts and mantle wedge fO2. J Petrol 55(12):2513–2536

Browne BL, Eichelberger JC, Patino LC, Vogel TA, Dehn J, Uto K, Hoshizumi H (2006) Generation of porphyritic and equigranular mafic enclaves during magma recharge events at Unzen Volcano, Japan. J Petrol 47(2):301–328

Bryant JA, Yogodzinski GM, Churikova TG (2007) Melt-mantle interactions beneath the Kamchatka arc: evidence from ultramafic xenoliths from Shiveluch volcano: G3. Geochem Geophys Geosyst 8(4):1–24

Churikova, T.G., Gordeychik, B.N., Ivanov, B.V., and Worner, G., 2013, Relationship between Kamen Volcano and the Klyuchevskaya group of volcanoes (Kamchatka): Journal of Volcanology and Geothermal Research, v. 263, p. 3–21.

Coogan LA, Saunders AD, Wilson RN (2014) Aluminum-in-olivine thermometry of primitive basalts: evidence of an anomalously hot mantle source for large igneous provinces. Chem Geol 368:1–10

Dalpé C, Baker DR (2000) Experimental investigation of large-ion-lithophile-element-, high-field-strength-element- and rare-earth-element-partitioning between calcic amphibole and basaltic melt: the effects of pressure and oxygen fugacity. Contrib Mineral Petrol 140(2):233–250

Danyushevsky LV (2001) The effect of small amounts of H_2O on crystallisation of mid-ocean ridge and backarc basin magmas. J Volcanol Geotherm Res 110:265–280

Davidson JP, Turner S, Plank T (2013) Dy/Dy*: variations arising from mantle sources and petrogenetic processes. J Petrol 54(3):525–537

Davydova VO, Shcherbakov VD, Plechov PY, Perepelov AB (2017) Petrology of Mafic enclaves in the 2006–2012 eruptive products of Bezymianny volcano, Kamchatka. Petrology 25(6):592–614

Delaney JS, Dyar MD, Sutton SR, Bajit S (1998) Redox ratios with relevant resolution: Solving an old problem by using the synchrotron microXANES probe. Geology 26(2):139–142

Dirksen O, Humphreys MCS, Pletchov P, Melnik O, Demyanchuk Y, Sparks RSJ, Mahony S (2006) The 2001–2004 dome-forming eruption of Shiveluch volcano, Kamchatka: observation, petrological investigation and numerical modelling. J Volcanol Geotherm Res 155:201–226

Dixon JE, Stolper EM, Holloway JR (1995) An experimental study of water and carbon dioxide solubilities in mid-ocean ridge basaltic liquids Part I: calibration solubility models. J Petrol 36(6):1607–1631

Donovan JJ, Tingle TN (1996) An improved mean atomic number background correction for quantitative microanalysis. J Microsc Soc Am 2(1):1–7

Donovan J, Kremser D, Fournelle J (2012) Probe for EPMA: acquisition, automation and analysis. Probe Software Inc., Oregon

Dyar MD, McGuire AV, Mackwell SJ (1992) Fe^{3+}/H^+ and D/H in kaersutites—misleading indicators of mantle source fugacities. Geology 20:565–568

Dyar MD, Mackwell SJ, McGuire AV, Cross LR, Robertson JD (1993) Crystal chemistry of Fe^{3+} and H^+ in mantle kaersutite: implications for mantle metasomatism. Am Mineral 78:968–979

Dyar MD, Breves EA, Gunter ME et al (2016) Use of multivariate analysis for synchrotron micro-XANES analysis of iron valence state in amphiboles. Am Mineral 101:1171–1189

Eggler DH (1976) Does CO_2 cause partial melting in the low-velocity layer of the mantle? Geology 4(2):69–72

Eggler DH (1978) The effect of CO_2 upon partial melting of peridotite in the system Na_2O-CaO-Al_2O_3-MgO-SiO_2-CO_2 to 35 kbar, with an analysis of melting in a peridotite-H_2O-CO_2 system. Am J Sci 278:305–343

Eichelberger JC (1975) Origin of andesite and dacite: evidence of mixing at Glass Mountain in California and at other circum-Pacific volcanoes. Geolog Soc Am Bull 86:1381–1391

Eichelberger JC, Chertkoff DG, Dreher ST, Nye CJ (2000) Magmas in collision: rethinking chemical zonation in silicic magmas. Geology 28(7):603–606

Eichelberger JC, Izbekov PE, Brown BL (2006) Bulk chemical trends at arc volcanoes are not liquid lines of descent. Lithos 87:135–154

Fedotov SA (1991) Active volcanoes of Kamchatka. Moscow Nauka Publishers, Moscow, vol. 1–2. pp. 415

Ferlito C (2011) Bimodal geochemical evolution at Sheveluch stratovolcano, Kamchatka, Russia: consequence of a complex subduction at the junction of the Kuril Kamchatka and Aleutian island arcs. Earth Sci Rev 105:49–69

Ferlito C, Lanzafame G (2010) The role of supercritical fluids in the potassium enrichment of magmas at Mount Etna volcano (Italy). Lithos 119(3–4):642–650

Fujimaki H, Tatsumoto M, Aoki K (1984) Partition coefficients of Hf, Zr, and REE between phenocrysts and groundmasses. J Geophys Res Solid Earth 89:B662–B672

Gavrilenko M, Herzberg C, Vidito C, Carr MJ, Tenner T, Ozerov A (2016) A Calcium-in-Olivine Geohygrometer and its Application to Subduction Zone Magmatism. J Petrol 57(9):1811–1832

Gavrilenko M, Ozerov A, Kyle PR, Carr MJ, Nikulin A, Vidito C, Danyushevsky LV (2016) Abrupt transition from fractional crystallization to magma mixing at Gorely volcano (Kamchatka) after caldera collapse. Bull Volcanol 78(47):1–28

Gavrilenko M, Krawczynski MJ, Ruprecht P, Li W, Catalano JG (2019) The quench control of water estimates in convergent margin magmas. Am Mineral 104(7):936–948

Ghiorso MS, Gualda GA (2015) An H_2O-CO_2 mixed fluid saturation model compatible with rhyolite-MELTS. Contrib Mineral Petrol 169(6):1–30

Golowin R, Portnyagin M, Hoernle K, Sobolev A, Kuzmin D, Werner R (2017) The role and conditions of second-stage mantle melting in the generation of low-Ti tholeiites and boninites: the case of Manihiki Plateau and the Troodos ophiolite. Contrib Mineral Petrol 172(11–12):104

Gorbach NV, Portnyagin M (2011) Geology and petrology of the lava complex of young Shiveluch Volcano, Kamchatka. Petrology 19(2):134–166

Gorbach NV, Portnyagin M, Tembrel I (2013) Volcanic structure and composition of Old Shiveluch volcano, Kamchatka. J Volcanol Geotherm Res 263:193–208

Gorbach N, Portnyagin MV, Philosofova T (2016) Dynamics of extrusive dome growth and variations in chemical and mineralogical composition of Young Shiveluch andesites in 2001–2013. J Volcanol Seismol 10(6):360–381

Gordeychik BN, Churikova TG, Kronz A, Sundermeyer C, Simakin A, Wörner G (2018) Growth of, and diffusion in, olivine in ultra-fast ascending basalt magmas from Shiveluch volcano. Sci Rep 8(1):1–15

Grove TL, Elkins-Tanton LT, Parman SW, Chatterjee N, Muntener O, Gaetani GA (2003) Fractional crystallization and mantle-melting controls on calc-alkaline differentiation trends. Contrib Mineral Petrol 145:515–533

Grove TL, Baker MB, Price RC, Parman SW, Elkins-Tanton LT, Chatterjee N, Muntener O (2005) Magnesian andesite and dacite lavas from Mt. Shasta, northern California: products of fractional crystallization of H_2O-rich mantle melts. Contrib Mineral Petrol 148:542–565

Grove TL, Till CB, Krawczynski MJ (2012) The role of H_2O in subduction zone magmatism. Ann Rev Earth Planet Sci 40:413–439

Halama R, Boudon G, Villemant B, Joron J, LeFriant A, Komorowksi J (2006) Pre-eruptive crystallization conditions of mafic and silicic magmas at the plat pays volcanic complex, Dominica (Lesser Antilles). J Volcanol Geotherm Res 153:200–220

Helz RT (1973) Phase relations of basalts in their melting range at P_{H2O} = 5 kb as a function of oxygen fugacity, Part I. Mafic phases. J Petrol 14(2):249–302

Hochstaedter AG, Kepezhinskas P, Defant M, Drummond M, Koloskov A (1996) Insights into the volcanic arc mantle wedge from magnesian lavas from the Kamchatka arc. J Geophys Res 101(B1):697–712

Holland T, Blundy J (1994) Non-ideal interactions in calcic amphiboles and their bearing on amphibole-plagioclase thermometry. Contrib Mineral Petrol 116:433–447

Holloway JR (2004) Redox reactions in seafloor basalts: possible insights into silicic hydrothermal systems. Chem Geol 210(1–4):225–230

Humphreys MCS, Blundy JD, Sparks RSJ (2006) Magma evolution and open-system processes at Shiveluch Volcano: insights from phenocryst zoning. J Petrol 47(12):2303–2334

Humphreys MCS, Blundy JD, Sparks RSJ (2008) Shallow-level decompression crystallisation and deep magma supply at Shiveluch Volcano. Contrib Mineral Petrol 155:45–61

Humphreys MCS, Brooker RA, Fraser DG, Burgisser A, Mangan MT, McCammon C (2015) Coupled interactions between volatile activity and Fe oxidation state during arc crustal processes. J Petrol 56(4):795–814

Ishikawa T, Tera F, Nakazawa T (2001) Boron isotope and trace element systematics of the three volcanic zones in the Kamchatka arc. Geochim Cosmochim Acta 65(24):4523–4537

Iwasaki T, Levin V, Nikulin A, Iidaka T (2013) Constraints on the Moho in Japan and Kamchatka. Tectonophysics 609:184–201

Izbekov PE, Eichelberger JC, Ivanov BV (2004) The 1996 Eruption of Karymsky Volcano, Kamchatka: historical record of basaltic replenishment of an Andesite Reservoir. J Petrol 45(11):2325–2345

Jagoutz O, Muntener O, Schmidt MW, Burg J (2011) The roles of flux- and decompression melting and their respective fractionation lines for continental crust formation: Evidence from the Kohistan arc. Earth Planet Sci Lett 303(1–2):25–36

Jarosewich E, Nelen JA, Norberg JA (1980) Reference samples for electron microprobe analysis. Geostand Newsl 4(1):43–47

Johnson KTM (1994) Experimental cpx and garnet melt partitioning of REE and other trace elements at high pressures; petrogenetic implications. Mineralog Mag 58:454–455

Johnson DM, Hooper PR, Conrey RM (1999) XRF analysis of rocks and minerals for major and trace elements on a single low dilution Li-tetraborate fused bead. Adv X-ray Anal 41:843–867

Kamenetsky VS, Pompilio M, Métrich N, Sobolev AV, Kuzmin DV, Thomas R (2007) Arrival of extremely volatile-rich

high-Mg magmas changes explosivity of Mount Etna. Geology 35(5):255–258
Kelley KA, Cottrell E (2012) The influence of magmatic differentiation on the oxidation state of Fe in a basaltic arc magma. Earth Planet Sci Let 329–330:109–121
King PL, Hervig RL, Holloway JR, Vennemann TW, Righter K (1999) Oxy-substitution and dehydrogenation in mantle-derived amphibole megacrysts. Geochim Cosmochim Acta 63(21):3635–3651
King PL, Hervig RL, Holloway JR, Delaney JS, Dyar MD (2000) Partitioning of Fe^{3+}/Fe_{total} between amphibole and basanitic melt as a function of oxygen fugacity. Earth Planet Sci Let 178:97–112
Knaack C, Cornelius S, Hooper P (1994) Trace element analyses of rocks and minerals by ICP-MS: open file report. Department of Geology, Washington State University
Kocak K, Isik F, Arslan M, Zedef V (2005) Petrological and source region characteristics of ophiolitic hornblende gabbros from the Aksaray and Kayseri regions, central Anatolian crystalline complex, Turkey. J Asian Earth Sci 25:883–891
Krawczynski MJ, Grove TL, Behrens H (2012) Amphibole stability in primitive arc magmas: effects of temperature, H_2O content, and oxygen fugacity. Contrib Mineral Petrol 164:317–339
Kress VC, Carmichael ISE (1991) The compressibility of silicate liquids containing Fe_2O_3 and the effect of composition, temperature, oxygen fugacity, and pressure on their redox states. Contrib Mineral Petrol 108(1–2):82–92
Kushiro I, Mysen BO (2002) A possible effect of melt structure on the $Mg\text{-}Fe^{2+}$ partitioning between olivine and melt. Geochim Cosmochim Acta 66(12):2267–2272
Larocque J, Canil D (2010) The role of amphibole in the evolution of arc magmas and crust: the case from the Jurassic Bonanza arc section, Vancouver Island, Canada. Contrib Miner Petrol 159:475–492
Leake BE, Woolley AR, Arps CES et al (1997) Nomenclature of amphiboles: report of the subcommittee on amphiboles of the International Mineralogical Association, Commission of New Minerals and Mineral Names. Am Mineral 82:1019–1037
Lee CA, Luffi P, Plank T, Dalton H, Leeman WP (2009) Constraints on the depths and temperatures of basaltic magma generation on Earth and other terrestrial planets using new thermobarometers for mafic magmas. Earth Planet Sci Lett 279(1–2):20–33
Martin VM, Holness MB, Pyle DM (2006) Textural analysis of magmatic enclaves from the Kameni Islands, Santorini, Greece. J Volcanol Geoth Res 154:89–102
Martin VM, Morgan DJ, Jerram DA, Caddick MJ, Prior DJ, Davidson JP (2008) Bang! month-scale eruption triggering at Santorini Volcano. Science 321(5893):1178
Mathez EA (1984) Influence of degassing on oxidation states of basaltic magmas. Nature 310:371–375
Mironov N, Portnyagin MV, Botcharnikov RE, Gurenko A, Hoernle K, Holtz F (2015) Quantification of the CO_2 budget and $H_2O\text{-}CO_2$ systematics in subduction-zone magmas through the experimental hydration of melt inclusions in olivine at high H_2O pressure. Earth Planet Sci Lett 425:1–11
Mitchell AL, Gaetani GA, O'Leary JA, Hauri EH (2017) H_2O solubility in basalt at upper mantle conditions. Contrib Mineral Petrol 172(85):1–16
Moore G, Vennemann TW, Carmichael ISE (1998) An empirical model for the solubility of H_2O in magmas to 3 kbar. Am Mineral 83(1):36–42
Moore LR, Gazel W, Tuohy R et al (2015) Bubbles matter: an assessment of the contribution of vapor bubbles to melt inclusion volatile budgets. Am Miner 199(4):806–823
Moussallam Y, Edmonds M, Scaillet B, Peters N, Gennaro E, Sides I, Oppenheimer C (2016) The impact of degassing on the oxidation state of basaltic magmas: a case study of Kilauea volcano. Earth Planet Sci Lett 450:317–325
Nikulin A, Levin V, Shuler A, West M (2010) Anomaloug seismic structure beneath the Klyuchevskoy Group, Kamchatka. Geophys Res Lett 37(14)
Nikulin A, Levin V, Carr M, Herzberg C, West M (2012) Evidence for two upper mantle sources driving volcanism in Central Kamchatka. Earth Planet Sci Lett 321:14–19
Papale P, Moretti R, Barbato D (2006) The compositional dependence of the saturation surface of $H_2O + CO_2$ fluids in silicate melts. Chem Geol 229(1–3):78–95
Parlak O, Hock V, Delaloye M (2000) Suprasubduction zone origin of the Pozanti-Karsanti Ophiolite (southern Turkey) deduced from whole-rock and mineral chemistry of the gabbroic cumulates. In: Bozkurt E, Winchester JA, Piper JDA (eds) Tectonics and magmatism in Turkey and the surrounding area, vol 137. Geological Society of London, London, pp 219–234
Parman SW, Grove TL, Kelley KA, Plank T (2011) Along-arc variations in the pre-eruptive H_2O contents of mariana arc magmas inferred from fractionation paths. J Petrol 52(2):257–278
Paster TP, Schauwecker DS, Haskin LA (1974) The behavior of some trace elements during solidification of the Skaergaard layered series. Geochim Cosmochim Acta 38(10):1549–1577
Plail M, Barclay J, Humphreys MCS, Edmonds M, Herd RA, Christopher TE (2014) Characterization of mafic enclaves in the erupted products of Soufrière Hills Volcano, Montserrat, 2009 to 2010. In: Wadge G, Robertson REA, Voight B (eds) The eruption of Soufrière Hills Volcano, Montserrat from 2000 to 2010. Geological Society of London, London, Memoirs. vol. 39, pp. 343–360
Plail M, Edmonds M, Woods AW, Barclay J, Humphreys MCS, Herd RA, Christopher T (2018) Mafic enclaves record syn-eruptive basalt intrusion and mixing. Earth Planet Sci Lett 484:30–40
Plank T, Manning CE (2019) Subducting carbon. Nature 574(7778):343–352
Ponomareva VV, Melekescev IV, Braitsva O, Churikova TG, Pevzner M, Sulerzhitsky L (2007a) Late pleistocene-holocene volcanism on the Kamchatka Peninsula, Northwest Pacific Region. In: Eichelberger JC, Gordeev E, Izbekov PE, Kasahara M, Lees J (eds) Volcanism and subduction: the Kamchatka Region. American Geophysical Union. vol. 172, pp. 165–198
Ponomareva V, Kyle P, Pevzner M, Sulerzhitsky L, Hartman M (2007b) Holocene eruptive history of Shiveluch Volcano, Kamchatka Peninsula, Russia. In: Eichelberger JC, Gordeev E, Izbekov PE, Kasahara M, Lees J (eds) Volcanism and subduction: the Kamchatka Region. American Geophysical Union. vol. 172, pp. 263–282
Ponomareva V, Portnyagin MV, Pevzner M, Blaauw M, Kyle P, Derkachev A (2015) Tephra from andesitic Shiveluch volcano, Kamchatka, NW Pacific: chronology of explosive eruptions and geochemical fingerprinting of volcanic glass. Int J Earth Sci 104:1459–1482
Portnyagin M, Bindeman I, Hoernle K, Hauff F (2007) Geochemistry of primitive lavas of the Central Kamchatka depression: magma generation at the edge of the pacific plate. In: Eichelberger JC, Gordeev E, Izbekov PE, Kasahara M, Lees J (eds) Volcanism and subduction: the Kamchatka Region, American Geophysical Union. vol. 172, pp. 199–239
Putirka KD (2008) Thermometers and barometers for volcanic systems. Rev Mineral Geochem 69(1):61–120
Ridolfi F, Renzulli A, Puerini M (2010) Stability and chemical equilibrium of amphibole in calc-alkaline magmas: an overview, new thermobarometric formulations and application to subduction-related volcanoes. Contrib Mineral Petrol 150:45–66
Ruprecht P, Bachmann O (2010) Pre-eruptive reheating during magma mixing at Quizapu volcano and the implications for the explosiveness of silicic arc volcanoes. Geology 38(10):919–922

Ruprecht P, Bergantz GW, Cooper KM, Hildreth W (2012) The crustal magma storage system of Volcán Quizapu, Chile, and the effects of magma mixing on magma diversity. J Petrol 53(4):801–840

Shinohara H (2013) Volatile flux from subduction zone volcanoes: insights from a detailed evaluation of the fluxes from volcanoes in Japan. J Volcanol Geotherm Res 268:46–63

Shishkina TA, Botcharnikov RE, Holtz F, Almeev RR, Portnyagin MV (2010) Solubility of H_2O- and CO_2-bearing fluids in tholeiitic basalts at pressures up to 500 MPa. Chem Geol 277:115–125

Sisson TW, Grove TL (1993) Experimental investigations of the role of H_2O in calc-alkaline differentiation and subduction zone magmatism. Contrib Mineral Petrol 113:143–166

Sun SS, McDonough WF (1989) Chemical and isotopic systematics of oceanic basalts: implications for mantle composition and processes. Geolog Soc Lond Spl Publ 42:313–345

Tolstykh ML, Pevzner M, Naumov VB, Babanskii AD, Kononkova NN (2015) Types of parental melts of pyroclastic rocks of various structural–age complexes of the Shiveluch Volcanic Massif, Kamchatka: evidence from inclusions in minerals. Petrology 23(5):480–517

Vigouroux N, Wallace PJ, Kent AJR (2008) Volatiles in high-K magmas from the western Trans-Mexican volcanic belt: evidence for fluid fluxing and extreme enrichment of the mantle wedge by subduction processes. J Petrol 49(9):1589–1618

Volynets ON (1991) Geochemical types, petrology, and genesis of late cenozoic volcanic rocks from the Kurile-Kamchatka Island-Arc system. Intern Geol Rev 36:373–405

Volynets ON, Ponomareva V, Babansky AD (1997) Magnesian basalts of Shiveluch Andesite Volcano, Kamchatka. Petrology 5(2):206–221

Wallace PJ (2005) Volatiles in subduction zone magmas: concentrations and fluxes based on melt inclusion and volcanic gas data. J Volcanol Geoth Res 140(1–3):217–240

Wallace PJ, Kamenetsky VS, Cervantes P (2015) Melt inclusion CO_2 contents, pressures of olivine crystallization, and the problem of shrinkage bubbles. Am Mineral 100(4):787–794

Wan Z, Coogan LA, Canil D (2008) Experimental calibration of aluminum partitioning between olivine and spinel as a geothermometer. Am Mineral 93(7):1142–1147

Waters LE, Lange RA (2016) No effect of H_2O degassing on the oxidation state of magmatic liquids. Earth Planet Sci Lett 447:48–59

Watson EB, Green TH (1981) Apatite/liquid partition coefficients for the rare earth elements and strontium. Earth Planet Sci Lett 56:405–421

Wyllie PJ, Huang W (1976a) High CO_2 solubilities in mantle magmas. Geology 4(1):21–24

Wyllie PJ, Huang W (1976b) Carbonation and melting reactions in the system CaO-MgO-SiO_2-CO_2 at mantle pressures with geophysical and petrological applications. Contrib Mineral Petrol 54:79–107

Yoder HSJ, Tilley CE (1962) Origin of basalt magmas: an experimental study of natural and synthetic rock systems. J Petrol 3(3):342–532